

Characterizing Distant Worlds with Asterodensity Profiling

David M. Kipping^{1,2}^{**}

¹*Harvard-Smithsonian Center for Astrophysics, 60, Garden Street, Cambridge, MA 02138*

²*Carl Sagan Fellow*

Accepted 2014 February 12. Received 2014 January 10; in original form 2013 November 4

ABSTRACT

Eclipsing systems, such as transiting exoplanets, allow one to measure the mean stellar density of the host star under various idealized assumptions. Asterodensity Profiling (AP) compares this density to an independently determined value in order to check the validity of the assumptions and ultimately derive useful parameters. Several physical effects can cause said assumptions to become invalid, with the most well-known example being the so-called photo-eccentric effect. In this work, we provide analytic expressions for five other effects which induce AP deviations: the photo-blend, -spot, -timing, -duration and -mass effects. We find that these effects can easily reproduce large AP deviations and so we caution that extracting the eccentricity distribution is only viable with careful consideration of the prior distributions for these other effects. We also re-investigate the photo-eccentric effect and derive a single-domain minimum eccentricity expression and the parameter range for which analytic formulae are valid. This latter result shows that the assumptions underlying the analytic model for the photo-eccentric effect break down for close-in, highly-eccentric planets, meaning that extreme care must be taken in this regime. Finally, we demonstrate that contaminated light fraction can be solved for, indicating that AP could be a potent tool for planet validation.

Key words: techniques: photometric — methods: analytical — asteroseismology — planet and satellites: fundamental parameters — eclipses

1 INTRODUCTION

Asterodensity profiling (AP) is a relatively new concept in the study of astronomical eclipses, such as transiting planets and eclipsing binaries, with the potential to constrain various properties of an eclipsing system using photometric data alone. AP exploits a well-known trick in the field of photometric eclipses that if an object transits across the face of a star multiple times, then one can measure the mean density of the host star, ρ_* , using Kepler's Third Law alone, under various idealized assumptions. This was first demonstrated in the pioneering work of Seager & Mallén-Ornelas (2003) and the most common application of this trick in the study of exoplanets has been to use the ρ_* measurement as a luminosity indicator

for stellar evolution models, in order to obtain physical dimensions for the host star (Sozzetti et al. 2007).

AP goes further than this though, by comparing the transit light curve derived stellar density, $\rho_{*,\text{obs}}$, to some independent measure of the same term, $\rho_{*,\text{true}}$, in order to test the validity of the idealized assumptions and ultimately extract information on the state the eclipsing system. If all of the idealized assumptions made in the definition of $\rho_{*,\text{obs}}$ are correct (Seager & Mallén-Ornelas 2003), then naturally one expects $(\rho_{*,\text{obs}}/\rho_{*,\text{true}}) = 1$ (to within the measurement uncertainties). Any deviation from unity implies that one or more of the idealized assumptions are invalid and the magnitude and direction of this deviation provide insights into the physical origin of the discrepancy. These idealized assumptions include (but are not limited to) an opaque planet, a spherical planet, a spherical star, non-variable transit shape, Ke-

* E-mail: dkipping@cfa.harvard.edu

plerian circular orbit and negligible blending from unresolved luminous objects.

The first usage of the term “asterodensity profiling” was by Kipping et al. (2012), who focussed on Multi-body Asterodensity Profiling (MAP) to constrain mutual orbital eccentricities. By focussing on systems with multiple transiting planets, several measurements of $\rho_{\star,\text{obs}}$ are obtained, allowing one to seek relative discrepancies in $\rho_{\star,\text{obs}}$, rather than the absolute discrepancy determined when $\rho_{\star,\text{true}}$ is known. MAP is particularly powerful since it makes no assumption about the true stellar density.

Although Kipping et al. (2012) briefly speculated that Single-body Asterodensity Profiling (SAP) would be plausible if a very tight constraint on $\rho_{\star,\text{true}}$ was available, such as that from asteroseismology, Dawson & Johnson (2012) proposed that even a loose prior on $\rho_{\star,\text{true}}$ would be sufficient to identify highly eccentric planets. Referring to the effect as the “photoeccentric effect”, the authors demonstrated the technique on the known eccentric planet HD 17156b obtaining $e = 0.71^{+0.16}_{-0.09}$ in good agreement with the radial velocity determination of $e = 0.67 \pm 0.08$. In later work, the same authors showed that the *Kepler* planetary candidate KOI-1474.01 has an eccentricity of $e = 0.81^{+0.10}_{-0.07}$, if the candidate is genuine (Dawson et al. 2012). In the case of ostensibly near-circular orbits, SAP provides less constraining determinations; for example Kipping et al. (2013) recently used SAP on Kepler-22b to determine $e = 0.13^{+0.36}_{-0.13}$ (we propose an explanation for this in §3.6).

We also note that variants of AP have been explored in the exoplanet literature, although they are not referred to as AP explicitly. Since $\rho_{\star,\text{obs}}$ is a function of the observed transit durations (as shown later in §2), several previous works have re-phrased the problem by looking for anomalous transit durations (e.g. Moorhead et al. 2011; Kane et al. 2012). One particularly powerful advantage of explicit AP is that $\rho_{\star,\text{true}}$ is a direct observable from the “gold standard” inference from asteroseismology, using the frequency spacing of pulsations modes (Ulrich 1986). In contrast, the “true” transit duration or maximum transit duration can, in general, only be inferred by invoking stellar evolution models since one needs to estimate the stellar radius, R_{\star} (Moorhead et al. 2011).

AP, and variants thereof, have so far been predominantly employed for constraining orbital eccentricities in both individual systems (e.g. Dawson & Johnson 2012; Dawson et al. 2012; Kipping et al. 2013) and with regard to the entire eccentricity distribution (e.g. Moorhead et al. 2011; Kane et al. 2012; Dawson et al. 2013). The former goal has a particularly important place with regard to assessing habitability of planetary candidates since eccentricity can have severe effects (Dressing et al. 2010). The latter is mostly concerned with testing planet-formation models (Ford & Rasio 2008; Jurić & Tremaine 2008; Socrates et al. 2012; Dong et al. 2013).

The importance of measuring eccentricities is there-

fore apparent; thus explaining the recent focus of applying AP for constraining eccentricities via the photoeccentric effect. However, relatively little work exists in the literature exploring the other physical effects which can lead to $(\rho_{\star,\text{obs}}/\rho_{\star,\text{true}}) \neq 1$. This absence of investigation is problematic since a circular orbit is not the only idealized assumption in the definition of $\rho_{\star,\text{obs}}$ which may be in error, and thus responsible for an observation that $(\rho_{\star,\text{obs}}/\rho_{\star,\text{true}}) \neq 1$. Critically, negating these other effects may lead to systematic errors in derived eccentricities or even completely erroneous conclusions about the state of a system. Additionally, the analytic expressions for AP are only approximate forms (Kipping et al. 2012), and yet the explicit valid range for their applicability remains unknown. The purpose of this work is to provide analytic expressions for several plausible alternative mechanisms by which AP can produce $(\rho_{\star,\text{obs}}/\rho_{\star,\text{true}}) \neq 1$ and define the exact parameter range for which these expressions may be reasonably employed without a significant loss of accuracy. We therefore aim to provide a foundational theoretical framework for this burgeoning field of study.

2 PRINCIPLES OF ASTERODENSITY PROFILING

2.1 Determining $\rho_{\star,\text{obs}}$

It is not the purpose of this work to provide a detailed introductory review of basic transit theory. Despite this, we here provide a brief synopsis of how the mean stellar density is derived in the context of the AP technique. Those interested in a more detailed pedagogical discussion are directed to Winn (2010).

Throughout this work, including all appendices, we make the fundamental assumption that any observed transits satisfy the criteria $0 < b < (1 - p)$ where b is the impact parameter of the transiting object of p is the ratio-of-radii between the transiting object and the host star. In the absence of limb-darkening, such a transit would be described as exhibiting a flat-bottom. Since $b > 0$ at times, then our fundamental assumption also enforces the condition that $p < 1$ at all times. This means our work does not include total eclipses caused by planets orbiting white dwarf stars for example (Agol 2011), yet for which there are no observed examples to date. Employing this fundamental assumption, a transit provides four basic observational parameters:

- δ_{obs} : the observed transit depth
- τ_{obs} : the observed time of transit minimum
- $T_{14,\text{obs}}$: the observed first-to-fourth contact transit duration
- $T_{23,\text{obs}}$: the observed second-to-third contact transit duration

The transit depth scales with the size of the transiting object and thus p_{obs} is easily recovered. Multiple epochs provide several τ_{obs} measurements which can be used to infer the orbital period of the transiting object,

P . The other two observables, $T_{14,\text{obs}}$ and $T_{23,\text{obs}}$, may be used to determine the observed impact parameter, b_{obs} , and the observed scaled semi-major axis of the orbit, $(a/R_*)_{\text{obs}}$, as demonstrated by Seager & Mallén-Ornelas (2003). Under the assumption of a spherical, opaque, dark planet on a Keplerian circular orbit transiting a spherical, unblended host star, Seager & Mallén-Ornelas (2003) showed that the transit durations would be given by

$$T_{\frac{14}{23}} = \frac{P}{\pi} \sin^{-1} \left[\sqrt{\frac{(1 \pm p)^2 - b^2}{(a/R_*)^2 - b^2}} \right]. \quad (1)$$

These expressions may be solved simultaneously for b and (a/R_*) . We refer to these expressions as the *observed* impact parameter and *observed* scaled semi-major axis since both terms are only valid under the various assumptions made thus far.

$$b_{\text{obs}}^2 \equiv \frac{(1 - p_{\text{obs}})^2 - \frac{\sin^2(T_{23,\text{obs}}\pi/P)}{\sin^2(T_{14,\text{obs}}\pi/P)}(1 + p_{\text{obs}})^2}{1 - \frac{\sin^2(T_{23,\text{obs}}\pi/P)}{\sin^2(T_{14,\text{obs}}\pi/P)}} \quad (2)$$

$$(a/R_*)_{\text{obs}}^2 \equiv \frac{(1 + p_{\text{obs}})^2 - b_{\text{obs}}^2[1 - \sin^2(T_{23,\text{obs}}\pi/P)]}{\sin^2(T_{23,\text{obs}}\pi/P)}. \quad (3)$$

It is now trivial to show that $\rho_{*,\text{obs}}$ is found using Kepler's Third Law:

$$\rho_{*,\text{obs}} \equiv \frac{3\pi(a/R_*)_{\text{obs}}^3}{GP^2}, \quad (4)$$

where G is the Gravitational constant. Equation 4 also assumes $M_P \ll M_*$ in addition to the previous assumptions and we use the equivalent symbol since the above represents a definition which we will use throughout this work. Note, that we refer to this density with the subscript “obs” for observed, whereas previous works have used the subscript “circ” for circular (e.g. Dawson & Johnson 2012; Kipping et al. 2012). The reason for this change is that, as demonstrated throughout this paper, numerous other idealized assumptions are made to derive Equation 4 in addition to a circular orbit and it is somewhat misleading to label the term with “circ” since it implies that this is the only relevant assumption.

It is important to stress that limb darkening parameters do not feature in the calculation of $\rho_{*,\text{obs}}$. In other words, $\rho_{*,\text{obs}}$ is not functionally dependent upon the limb darkening coefficients (LDCs) or profile; e.g. $\rho_{*,\text{obs}} \neq f(u_1, u_2)$ in the case of quadratic limb darkening. This can be understood on the basis that the LDCs do not affect the instant at which the planet’s projected disc contacts the star’s projected disc i.e. the contact points, since this is purely dynamical. Therefore, the transit durations, $T_{14,\text{obs}}$ and $T_{23,\text{obs}}$, are not affected by the LDCs in anyway. Since $\rho_{*,\text{obs}}$ depends solely upon p_{obs} , P , $T_{14,\text{obs}}$ & $T_{23,\text{obs}}$, then $\rho_{*,\text{obs}}$ must also be independent of the LDCs. In practice, one could arrive at the

wrong $\rho_{*,\text{obs}}$ by fixing the LDCs to some values which do not represent the truth. This would lead to a biased estimate of p_{obs} , $T_{14,\text{obs}}$ & $T_{23,\text{obs}}$, and consequently a biased estimate of $\rho_{*,\text{obs}}$. We therefore advocate careful selection of the priors in the LDCs and specifically suggest employing the non-informative prior basis set proposed in Kipping (2013), which will propagate the uncertainty of the LDCs into the derivation of $\rho_{*,\text{obs}}$. Essentially, this means that the derived $\rho_{*,\text{obs}}$ value loses precision but gains accuracy - a satisfactory compromise in most cases. Having established that it makes no difference to any of the derivations in this work whether we include/exclude limb darkening, many of the figures in this paper will negate it for the sake of clarity but once again we stress that it does not affect the validity of the derived expressions.

Finally, we note that the reason why we earlier stated that we will assume $b < (1 - p)$ at all times is evident from the above expressions, since T_{23} is undefined otherwise and thus it is not possible to calculate $\rho_{*,\text{obs}}$. Therefore, using the approach of Seager & Mallén-Ornelas (2003), one can only measure the light curve derived stellar density of a star if $b < (1 - p)$ and thus AP is only possible in such a regime.

2.2 Observations versus Truth

Ideally, the observed transit depth and durations are equivalent to the true values. In such a case, one should expect (to within the measurement uncertainties) that

$$\lim_{\text{idealized assumptions valid}} \left(\frac{\rho_{*,\text{obs}}}{\rho_{*,\text{true}}} \right) = 1.$$

However, as is shown in this work, there are many realistic conditions which do not satisfy the ideal transit assumptions made in Seager & Mallén-Ornelas (2003). Rather than seeing this as nuisance though, the principle of AP is to exploit the $(\rho_{*,\text{obs}}/\rho_{*,\text{true}})$ ratio to not only test the validity of the idealized assumptions but to actually infer properties of an eclipsing system by analysis of the magnitude and direction of any discrepancies (or lack thereof).

As mentioned earlier, either an independent measure of $\rho_{*,\text{true}}$ is required to perform the SAP variant or relative differences between multiple transiting object can be used to perform MAP.

2.3 Methodology for Analytic Derivations of AP Effects

There are many different physical scenarios which can cause a significant AP discrepancy (which we define as when $(\rho_{*,\text{obs}}/\rho_{*,\text{true}}) \neq 1$ at high significance). In this work, we attempt to derive analytic expressions for several important effects to aid observers interpreting such measurements. In general, an unaccounted for effect (dubbed a “photo-name effect” throughout this work)

will cause a systematic and constant deviation in either the depth or the duration such that $p_{\text{obs}} \neq p_{\text{true}}$, $T_{14,\text{obs}} \neq T_{14,\text{true}}$ and/or $T_{23,\text{obs}} \neq T_{23,\text{true}}$. Unaccounted-for periodic transit timing/duration/depth variations (TTV/TDV/TδV) induced by perturbing gravitational influences or starspots can be interpreted as a systematic, constant deviation in the composite transit light curve's durations and/or depth too, as shown later in §3.3, §3.4 & §3.5. Therefore, in general, one may derive $\rho_{*,\text{obs}}$ by considering it to be functionally dependent via:

$$\rho_{*,\text{obs}} [p_{\text{obs}}(p_{\text{true}}, \mathbf{X}), T_{14,\text{obs}}(T_{14,\text{true}}, \mathbf{X}), T_{23,\text{obs}}(T_{23,\text{true}}, \mathbf{X})],$$

where \mathbf{X} is a vector of arbitrary length representing the parameters which describe the unaccounted-for physical effect(s). In practice, one computes the expressions for p_{obs} , $T_{14,\text{obs}}$ and $T_{23,\text{obs}}$ and then uses Equations 2, 3 & 4 to analytically express $\rho_{*,\text{obs}}(p_{\text{true}}, b_{\text{true}}, \rho_{*,\text{true}})$. In practice, the derived expression is often extremely cumbersome and impractical and thus the major challenge of such work is a) finding a simplified, useful approximate expression by invoking various assumptions b) determining the exact conditions for which the associated assumptions are valid. These two goals and the described basic methodology guide the work which follows throughout this paper. In general, we do not provide detailed derivations in the main text for the sake of brevity, but all relevant derivations are included in detail in the appendices.

3 ASTERODENSITY PROFILING EFFECTS

3.1 The Photo-mass Effect

We begin our exploration of various AP effects by considering that the idealized assumption $M_{\text{transiter}} \ll M_{\star}$ is invalid (the masses of transiting object and star respectively). We note that Dawson & Johnson (2012) briefly commented on this possibility previously (see §4.3). As with the subsequent sections, we will assume that all of the other idealized assumptions remain valid in order to derive the consequences of the “photo-mass” effect in isolation. In general, a confirmed exoplanet will safely satisfy this criteria but planetary candidates cannot so easily be treated, since the observations could be of an eclipsing binary or a white/brown-dwarf with a high mass ratio. Including the $M_{\text{transiter}}$ term in the derivation of the stellar density returns the result

$$\rho_{*,\text{obs}} = \rho_{*,\text{true}} + p^3 \rho_{\text{transiter}}, \quad (5)$$

where $\rho_{\text{transiter}}$ is the mean density of the transiting object (usually this is a transiting planet but the expressions are valid for eclipsing binaries too). This result implies that

$$\left(\frac{\rho_{*,\text{obs}}}{\rho_{*,\text{true}}} \right) = 1 + p^3 \frac{\rho_{\text{transiter}}}{\rho_{*,\text{true}}}, \quad (6)$$

which we may re-express as

$$\left(\frac{\rho_{*,\text{obs}}}{\rho_{*,\text{true}}} \right)^{\text{PM}} = 1 + \frac{M_{\text{transiter}}}{M_{\star}}, \quad (7)$$

where we use the subscript “PM” as an acronym for the photo-mass effect. Negating the planetary mass therefore causes us to overestimate $(\rho_{*,\text{obs}}/\rho_{*,\text{true}})$. For a confirmed/validated exoplanet, this effect will be $\lesssim 1\%$ and thus is usually only minor. For eclipsing binaries masquerading as planetary candidates through blending, this effect will become order unity.

3.2 The Photo-blend Effect

One of the most critical assumptions in the derivation of $\rho_{*,\text{obs}}$ is that the brightness variations observed are due to the host star alone, which means that the star is unblended. Blend sources come in many varieties involving triple and binary stellar configurations (Torres et al. 2011; Hartman et al. 2011) as well as even self-blending due to a hot compact object such as a white-dwarf or even a hot-Jupiter (Kipping & Tinetti 2010). Blend sources are the astrophysical bottleneck in confirming/validating the thousands of planetary candidates found by the *Kepler Mission* (Morton & Johnson 2011; Fressin et al. 2011).

We define the blend factor, \mathcal{B} , in this work as the ratio of the total flux to that of the target’s flux, via

$$\mathcal{B} \equiv \frac{F_{\star} + F_{\text{blend}}}{F_{\star}}, \quad (8)$$

where F_{\star} is the flux received from the target and F_{blend} is the sum of all extra contaminating components. In Appendix A, we show that if we assume $(a/R_{\star})^2 \gg (1+p)^2$, the effect of a blend may be expressed as (see Equation A18):

$$\left(\frac{\rho_{*,\text{obs}}}{\rho_{*,\text{true}}} \right)^{\text{PB}} = \mathcal{B}^{-3/4} \left(\frac{(1 + \sqrt{\mathcal{B}} p_{\text{obs}})^2 - b_{\text{obs}}^2}{(1 + p_{\text{obs}})^2 - b_{\text{obs}}^2} \right)^{3/2}. \quad (9)$$

Equation 9 is maximized for $b_{\text{obs}} \rightarrow (1 - p_{\text{obs}})$ and $p_{\text{true}} \rightarrow 1$ and for a binary star scenario of $\mathcal{B} \simeq 2$, we estimate that the PB effect cause AP effects up to order-unity. The assumption made to derive Equation 9, $(a/R_{\star})^2 \gg (1+p)^2$, may also be expressed as

$$\left(\frac{P}{\text{days}} \right)^{4/3} \gg 0.389 \left(\frac{\rho_{*,\text{true}}}{\text{g cm}^3} \right)^{-2/3}. \quad (10)$$

It can be seen from the above that this condition should be satisfied for all but the very shortest of orbital periods (e.g. Kepler-78b; Sanchis-Ojeda et al. 2013). Since all blend sources must satisfy $\mathcal{B} > 1$ (there is no such thing as a negative flux source), then inspection of Equation 9 reveals that blends always cause one to underestimate the stellar density. In principle then, an independent measure of the stellar density can be used to

measure the blend factor \mathcal{B} by inverting Equation 9. As discussed in detail in Appendix A5, inverting Equation 9 yields a quadratic equation with two valid roots:

$$\begin{aligned} \mathcal{B}_{+-} = & \frac{1}{4p_{\text{obs}}^4} \left(-2p_{\text{obs}} + \left(\frac{\rho_{*,\text{obs}}}{\rho_{*,\text{true}}} \right)^{2/3} [(1+p_{\text{obs}})^2 - b_{\text{obs}}^2] \right. \\ & \pm \left[\left(p_{\text{obs}} \left[(2+p_{\text{obs}}) \left(\frac{\rho_{*,\text{obs}}}{\rho_{*,\text{true}}} \right)^{2/3} - 2 \right] \right. \right. \\ & \left. \left. + \left(\frac{\rho_{*,\text{obs}}}{\rho_{*,\text{true}}} \right)^{2/3} (1-b_{\text{obs}}^2) \right)^2 - 4p_{\text{obs}}^2 (1-b_{\text{obs}}^2) \right]^{1/2} \right). \end{aligned} \quad (11)$$

The \mathcal{B}_{+-} functions are plotted in Figure 1 for different input parameters. There are several key observations of the expression. Firstly, for a known p_{obs} and b_{obs} , $(\rho_{*,\text{obs}}/\rho_{*,\text{true}})$ is always bound by the range:

$$\left(\frac{\rho_{*,\text{obs}}}{\rho_{*,\text{true}}} \right)_{\min} \leq \left(\frac{\rho_{*,\text{obs}}}{\rho_{*,\text{true}}} \right) < \left(\frac{\rho_{*,\text{obs}}}{\rho_{*,\text{true}}} \right)_{\max}, \quad (12)$$

where

$$\left(\frac{\rho_{*,\text{obs}}}{\rho_{*,\text{true}}} \right)_{\min} = \left(\frac{2p_{\text{obs}}(1+\sqrt{1-b_{\text{obs}}^2})}{(1+p_{\text{obs}})^2 - b_{\text{obs}}^2} \right)^{3/2}, \quad (13)$$

$$\left(\frac{\rho_{*,\text{obs}}}{\rho_{*,\text{true}}} \right)_{\max} = 1. \quad (14)$$

Curiously then, there is both an upper and lower limit on the range of $\rho_{*,\text{obs}}$ values a blend can produce any observation outside of this range *cannot* be due to the photo-blend effect only.

The second important observation is although the solution for \mathcal{B} is bi-modal, it is actually uni-modal for most $(\rho_{*,\text{obs}}/\rho_{*,\text{true}})$ inputs. Specifically, as shown in Appendix A5, the \mathcal{B}_+ is unphysical most inputs. This is also illustrated in Figure 1 by the gray dotted line. In practice then, only a small range of parameter space is bi-modal, which occurs when:

$$\left(\frac{\rho_{*,\text{obs}}}{\rho_{*,\text{true}}} \right)_{\min} \leq \left(\frac{\rho_{*,\text{obs}}}{\rho_{*,\text{true}}} \right) < \left(\frac{\rho_{*,\text{obs}}}{\rho_{*,\text{true}}} \right)_{\mathcal{B}_+,\max}, \quad (15)$$

where

$$\left(\frac{\rho_{*,\text{obs}}}{\rho_{*,\text{true}}} \right)_{\mathcal{B}_+,\max} = \left(\frac{(4-b_{\text{obs}}^2)p_{\text{obs}}}{(1+p_{\text{obs}})^2 - b_{\text{obs}}^2} \right)^{3/2}. \quad (16)$$

In fact, as visible in Figure 1, this bi-modal range has zero volume as $b_{\text{obs}} \rightarrow 0$ since $(\rho_{*,\text{obs}}/\rho_{*,\text{true}})_{\min} = (\rho_{*,\text{obs}}/\rho_{*,\text{true}})_{\mathcal{B}_+,\text{crit}}$ in this limit. In summary then, we have:

$$\mathcal{B} = \begin{cases} \text{no roots} & \text{if } 0 < \left(\frac{\rho_{*,\text{obs}}}{\rho_{*,\text{true}}} \right) < \left(\frac{\rho_{*,\text{obs}}}{\rho_{*,\text{true}}} \right)_{\min} \\ \mathcal{B}_- \text{ or } \mathcal{B}_+ & \text{if } \left(\frac{\rho_{*,\text{obs}}}{\rho_{*,\text{true}}} \right)_{\min} < \left(\frac{\rho_{*,\text{obs}}}{\rho_{*,\text{true}}} \right) < \left(\frac{\rho_{*,\text{obs}}}{\rho_{*,\text{true}}} \right)_{\mathcal{B}_+,\text{crit}} \\ \mathcal{B}_- & \text{if } \left(\frac{\rho_{*,\text{obs}}}{\rho_{*,\text{true}}} \right)_{\mathcal{B}_+,\text{crit}} < \left(\frac{\rho_{*,\text{obs}}}{\rho_{*,\text{true}}} \right) < 1 \\ \text{no roots} & \text{if } 1 < \left(\frac{\rho_{*,\text{obs}}}{\rho_{*,\text{true}}} \right) < \infty \end{cases} \quad (17)$$

3.3 The Photo-spot Effect

Starspots, networks and plages are thought to form by stellar magnetic fields generated by cyclonic turbulence in the outer convection zone of cool stars penetrating the stellar atmosphere (Berdyugina 2005). Starspots are thought to be a particularly common outcome of this process and continuous photometric monitoring reveals their signature as rotational modulations, which has allowed for the determination of rotation periods for thousands of stars (Basri et al. 2011; Walkowicz & Basri 2013).

Whilst large spots which are occulted by the transiting object are easy to identify and remove, unocculted spots are more challenging and perturb the transit depth as pointed out by Czesla et al. (2009). We define the act of unocculted starspots perturbing the observed transit depth, and thus the observed stellar density, as the “photo-spot” effect.

Equation 9 reveals that since $\mathcal{B} \geq 1$ for all blend sources, then the effect of a blend is to underestimate the stellar density. However, as proved in Kipping (2012), the transit depth change due to unocculted starspots behave like a $\mathcal{B} < 1$ blend factor and actually enhance the transit depth. This would therefore cause an observer to measure $(\rho_{*,\text{obs}}/\rho_{*,\text{true}}) > 1$. Kipping (2012) showed that the effect of the transit depth is given by

$$\begin{aligned} \frac{\delta_{\text{obs}}}{\delta_{\text{true}}} &= \frac{F_*(\text{unspotted})}{F_*(\text{spotted})}, \\ \frac{\delta_{\text{obs}}}{\delta_{\text{true}}} &= \frac{1}{1 - A_{\text{spots}}}, \end{aligned} \quad (18)$$

where F_* is the flux from the star and the unspotted case corresponds to the flux an observer would see if one took the actual starspot population and shrunk their sizes to zero. The second line re-writes this expression by defining A_{spots} as the effective normalized photometric amplitude of the rotational modulations. For a rotating star with one to a few major spots, there will be times when all of the spots in view and times when no spots are present, giving rise to quasi-periodic transit depth variations ($T\delta V$). We assume such a rotation period a) much longer than the transit duration, b) much shorter than the baseline of observations and c) has no commensurability with the transiting body’s orbital period. If we treat $F_*(\text{spotted})$ as behaving like a Fourier series of harmonic components, then the average effect on the transit depths (i.e. the folded transit light curve depth) would be

$$\bar{\delta}_{\text{obs}} \simeq \frac{1}{1 - A_{\text{spots}}/2}, \quad (19)$$

The photo-spot effect is illustrated in Figure 2, where the $T\delta V$ s give rise an apparently increased depth in the folded light curve. The depth ratio, $(\bar{\delta}_{\text{obs}}/\delta_{\text{true}})$, is equivalent to \mathcal{B}^{-1} using our definition of the blend factor in Equation 8. Exploiting this trick, one may write that a spot behaves like a blend with a blend factor, $\mathcal{B}_{\text{spot}}$, given by

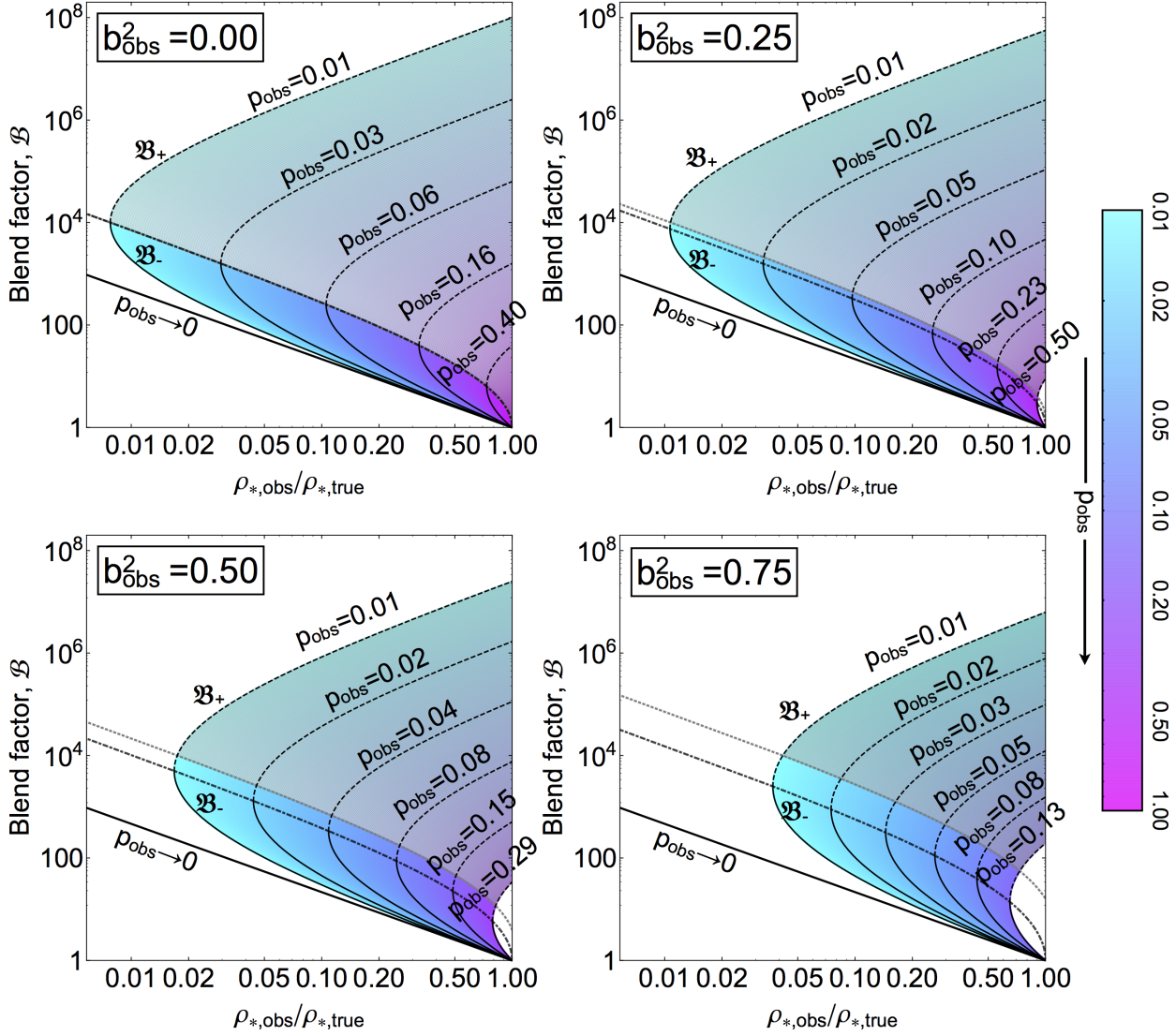


Figure 1. The Photo-blend Effect: Blends, or uncorrected contaminated light, always cause one to underestimate the stellar density, plotted here on the x -axis as $(\rho_{*,\text{obs}}/\rho_{*,\text{true}})$. One may solve for the blend factor, \mathcal{B} , to aid in validating candidate planets, yielding two analytic roots shown by the curved black (\mathcal{B}_+) and black-dashed (\mathcal{B}_-) lines for a range of apparent impact parameters, b_{obs} , and ratio-of-radii, p_{obs} . The \mathcal{B}_+ root is only physically valid between the point of inflection of the contours (traced by the black dot-dashed line) and the dotted gray line.

$$\begin{aligned} \mathcal{B}_{\text{spot}} &\simeq 1 - \frac{A_{\text{spots}}}{2}, \\ \mathcal{B}_{\text{spot}} &\simeq \frac{1}{2} \left(1 + \frac{F_{*}(\text{spotted})}{F_{*}(\text{unspotted})} \right). \end{aligned} \quad (20)$$

Equipped with Equation 20, one may now compute the consequences on the stellar density using the same expressions derived earlier for the photo-blend effect in §3.2.

$$\left(\frac{\rho_{*,\text{obs}}}{\rho_{*,\text{true}}} \right)^{\text{PS}} = \lim_{\mathcal{B} \rightarrow \mathcal{B}_{\text{spot}}} \left(\frac{\rho_{*,\text{obs}}}{\rho_{*,\text{true}}} \right)^{\text{PB}} \quad (21)$$

We note that plotting the \mathcal{B}_+ root for $(\rho_{*,\text{obs}}/\rho_{*,\text{true}}) > 1$ again yields unphysically high blend factors (and always $\mathcal{B} > 1$ which is not possible from the photo-spot effect). Therefore, one only need consider the \mathcal{B}_- root for the photo-spot effect. As with the photo-blend effect, the same conditions apply for the application of these analytic photo-spot equations:

$$\left(\frac{P}{\text{days}}\right)^{4/3} \gg 0.389 \left(\frac{\rho_{*,\text{true}}}{\text{g cm}^3}\right)^{-2/3}. \quad (22)$$

Typically, even a heavily spotted star will be in the range $A_{\text{spots}} \lesssim 20\%$ and usually $\lesssim 1\%$. Therefore spots affect the ratio $(\rho_{*,\text{obs}}/\rho_{*,\text{true}})$ at the same order-of-magnitude level as the normalized rotational modulations amplitude. The maximum AP deviation via this effect can be evaluated by computing the limit for $b_{\text{obs}} \rightarrow (1-p_{\text{obs}})$ and $p_{\text{true}} \rightarrow 1$. For an extreme 20% spot amplitude we obtain an AP effect of order $\mathcal{O}[10^{-1}]$, and for a typical 1% spot amplitude this becomes $\mathcal{O}[10^{-2}]$. In principle, it is possible to correct for the photo-spot effect using rotational modulation data, although this can be challenging (Kipping 2012) and such effort should be put in the context of the expected magnitude of this effect.

3.4 The Photo-timing Effect

Transit timing variations (TTVs) have been revealed by the *Kepler Mission* to be a fairly common occurrence in planetary systems (Ford et al. 2012; Mazeh et al. 2013) with $\sim 10\%$ showing significant TTVs. TTVs of low amplitude can be difficult to infer by fitting individual transits and yet if we ignore their presence they will systematically bias the derived transit parameters. An object with low-amplitude TTVs ($A_{\text{TTV}} < T_{23}$) with $N \gg 1$ cycles over the baseline of continuous transit observations will cause a naively folded transit light curve to appear smeared out, as illustrated in Figure 3. The four contact points appear shifted due to the motion of the planet leading to erroneously derived T_{23} and T_{14} durations. Naturally, this will feed into the derived impact parameter, scaled semi-major axis and light curve derived stellar density.

In Appendix D, we derive the full consequences of unaccounted TTVs on the derived transit parameters. The effect on ρ_* depends upon the true impact parameter but unfortunately the impact parameter is also corrupted by the TTVs. One way round this is to consider the worst-case scenario where $\rho_{*,\text{obs}}$ is most discrepant from $\rho_{*,\text{true}}$, which occurs for $b = 0$. In this case, one finds a simple form for the photo-timing effect:

$$\left(\frac{\rho_{*,\text{obs}}}{\rho_{*,\text{true}}}\right)^{\text{PT}} \geq \left(\frac{p}{p + nA_{\text{TTV}}(a/R_*)}\right)^{3/2}, \quad (23)$$

where $n = 2\pi/P$, $2A_{\text{TTV}}$ is the peak-to-peak TTV amplitude, (a/R_*) implicitly refers to $(a/R_*)_{\text{true}}$ and we use the \geq symbol since the calculation is computed for the extreme case of $b = 0$. In Appendix D, we show that this expression is a valid approximation for:

$$(a/R_*)^2 \gg 2, \quad (24)$$

$$2A_{\text{TTV}} \ll T_{23}. \quad (25)$$

The first condition may also be re-expressed in physical units as

$$\left(\frac{P}{\text{days}}\right)^{4/3} \gg 0.231 \left(\frac{\rho_{*,\text{true}}}{\text{g cm}^3}\right)^{-2/3}. \quad (26)$$

In general, one expects TTVs to be detectable by careful inspection of the data. In the case that significant TTVs are present, an accurate light curve derived stellar density could be derived by either using a model which allows for unique transit times or using a physical model which accounts for TTVs (i.e. a photodynamical model), provided the model well-explains the data.

If no significant TTVs are detected, or an observer opts to try and remove the best-fitting TTVs and then re-fit assuming a linear ephemeris, the light curve derived stellar density can still be affected by unseen low-amplitude TTVs. In principle, one expects to be able to exclude TTVs up to some maximum amplitude level to 1-, 2-, 3- (etc) σ confidence. In essence, this means that the uncertainty on $\rho_{*,\text{obs}}$ will be underestimated. However, using our expressions, it is possible to quantify this unaccounted-for uncertainty in the extreme case occurring for $b_{\text{true}} = 0$:

$$\sigma_{(\rho_{*,\text{obs}}/\rho_{*,\text{true}})} \lesssim 7.5 \frac{G^{1/3} \rho_{*,\text{obs}}^{1/3}}{p P^{1/3}} \frac{\sigma_\tau}{N^{1/4}}, \quad (27)$$

where σ_τ is the typical timing uncertainty on each transit and N is the number of transits observed. As an example, consider a planet with $P = 10$ days, $p = 0.1$ around a Solar-like star. Consider that each transit can be timed to a precision of 1 minute and that over a span of 4 years the target is continuously monitored. This would give $\sigma_{(\rho_{*,\text{obs}}/\rho_{*,\text{true}})}^{\text{max}} \lesssim 9\%$. Once again, we emphasize that this error would not be normally propagated into the uncertainty on $\rho_{*,\text{obs}}$. This demonstrates the photo-timing effect leads to inflated errors on the stellar density and caution must be taken in interpreting small discrepancies. For much larger timing errors of $\sigma_\tau \simeq 10$ minutes, the effect can be estimated to be $\mathcal{O}[10^0]$.

3.5 The Photo-duration Effect

Transit durations variations (TDVs) are another example of a dynamical effect which will alter the shape of a folded transit light curve, if left unaccounted for. TDVs were first posited to be a signature of exomoons (Kipping 2009a,b) but have since been demonstrated to be also possible in strongly interacting multi-planet systems too (Nesvorný et al. 2012). TDVs come in two flavors, velocity-induced transit duration variations, TDV-V, and transit impact parameter induced transit duration variations, TDV-TIP (Kipping 2009a,b). In this work, we focus on the more dominant component of TDV-V.

TDV-Vs essentially stretch and squash the width of the transit shape and a well sampled periodic set of light curves with TDV-Vs will exhibit a deformed folded transit shape, if neglected. This is illustrated in Figure 4,

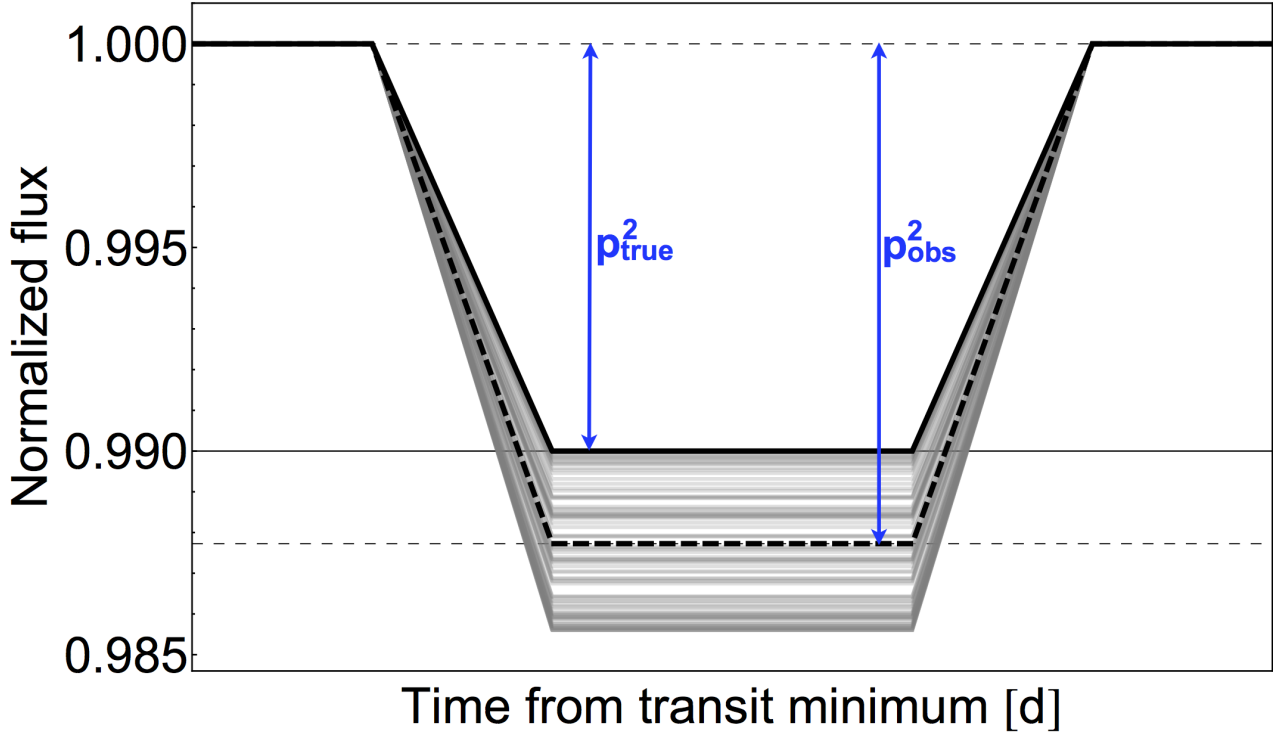


Figure 2. *The Photo-spot Effect:* By neglecting to correct for transit depth variations ($T\delta V$) due to unocculted spots, a folded transit light curve will exhibit deformation leading to the erroneous retrieval of the basic transit parameters, including the observed stellar density, $\rho_{\star,\text{obs}}$. Here, the black line represents the true original signal, the gray lines are 100 examples of the signal with unaccounted for sinusoidal $T\delta V$ s and the black-dashed line is the naively folded transit light curve, exhibiting sizable deformation.

where the composite light curve is deformed in a similar way to that caused by periodic TTVs earlier in Figure 3. We consider the TDVs to be due to the velocity of a planet varying periodically between the extrema of $v_{\min} = v_0(1 - A_{\text{TDV}})$ and $v_{\max} = v_0(1 + A_{\text{TDV}})$, where the “0” subscript denotes the parameter’s value in the absence of TDVs. Since the durations are inversely proportional to the velocity of the planet, then the durations vary over time t over the range:

$$T_{23,0}^{14}(1 - A_{\text{TDV}}) \leq T_{23}^{14}(t) \leq T_{23,0}^{14}(1 + A_{\text{TDV}}). \quad (28)$$

The A_{TDV} term therefore defines the relative changes in the duration, and not the absolute changes, which is the more natural expression of TDV-Vs. Using this model, we derive the effect of periodic TDVs on the light curve derived stellar density in Appendix E to be:

$$\left(\frac{\rho_{\star,\text{obs}}}{\rho_{\star,\text{true}}}\right)^{\text{PD}} = \left(\frac{(a/R_{\star})^2 p + 4A_{\text{TDV}}^2 b^2 p + 2A_{\text{TDV}}[(1-p^2)^2 - b^2(1+p^2)]}{(a/R_{\star})^2[p + 4A_{\text{TDV}}^2 p + 2A_{\text{TDV}}(1+p^2-b^2)]}\right)^{3/2} \quad (29)$$

where (a/R_{\star}) is $(a/R_{\star})_{\text{true}}$ and can be estimated as $[(GP^2\rho_{\star})/(3\pi)]^{1/3}$. In Appendix E, we show that the above is valid when

$$(a/R_{\star})^2 \gg 2, \quad (30)$$

$$A_{\text{TDV}} \ll 1. \quad (31)$$

As with the photo-timing effect, the photo-duration effect can be thought of as imparting an error term on the observed stellar density. We are unable to find a simple form for the resulting expression though and so suggest observers use:

$$\sigma_{(\rho_{\star,\text{obs}}/\rho_{\star,\text{true}})}^{\text{PD}} = 1 - \left[\lim_{A_{\text{TDV}} \rightarrow \sigma_{A_{\text{TDV}}}} \left(\frac{\rho_{\star,\text{obs}}}{\rho_{\star,\text{true}}} \right)^{\text{PD}} \right]. \quad (32)$$

As with the photo-timing effect error, we demonstrate the above by considering the same example of a planet with $P = 10$ days, $p = 0.1$ around a Solar-like star with $b = 0$ ($T_{14,0} = 4.3$ hours). Timing each transit to 1 minute precision, which corresponds to an approximately 2 minute duration uncertainty, over 4 years of continuously monitoring gives $\sigma_{(\rho_{\star,\text{obs}}/\rho_{\star,\text{true}})}^{\text{max}} = 10.6\%$.

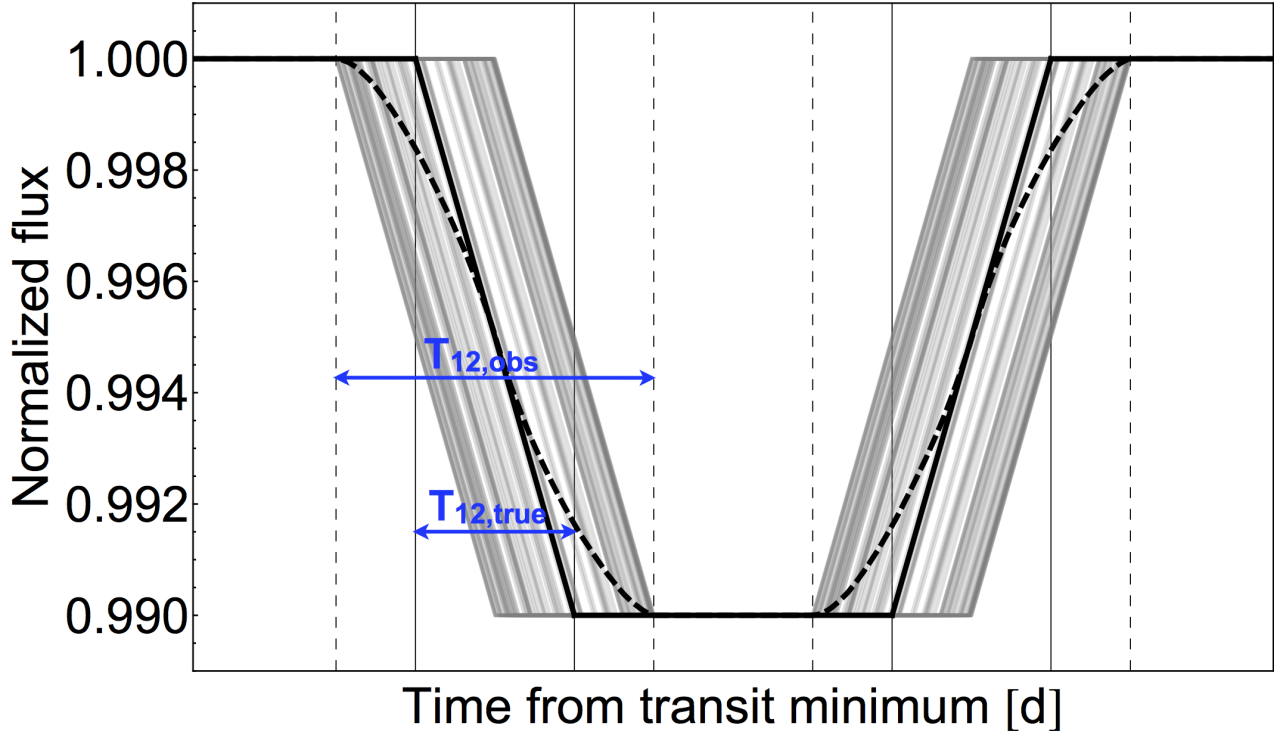


Figure 3. *The Photo-timing Effect:* If even low-amplitude transit timing variations (TTV) are negated, a folded transit light curve will exhibit deformation leading to the erroneous retrieval of the basic transit parameters, including the observed stellar density, $\rho_{\star,\text{obs}}$. Here, the black line represents the true original signal, the gray lines are 100 examples of the signal with unaccounted for sinusoidal TTVs and the black-dashed line is the naively folded transit light curve, exhibiting sizable deformation.

Therefore, in this example, the photo-duration effect imparts approximately the same level of uncertainty into the observed stellar density as the photo-timing effect does. However, unlike TTVs, TDVs are considerably rarer in the database of known exoplanets with only a few examples and so the a-priori probability of hidden TDVs is clearly distinct to that from timing variations.

3.6 The Photo-eccentric Effect

3.6.1 General effect

The effect of eccentricity is the most well-studied asterodensity profiling effect. Dawson & Johnson (2012) refer to this asterodensity profiling effect as the “photo-eccentric effect”, as we do so here. The first explicit derivation of the effect of eccentricity is given in Kipping et al. (2012) who find

$$\left(\frac{\rho_{\text{obs}}}{\rho_{\text{true}}}\right)^{\text{PE}} = \Psi, \quad (33)$$

where

$$\Psi \equiv \frac{(1 + e \sin \omega)^3}{(1 - e^2)^{3/2}}. \quad (34)$$

Despite the expression already existing in the literature, we are unaware of any investigations regarding the range of parameters which the *approximation* shown in Equation 33 is valid. In Appendix B, we present a detailed investigation of this and surmise that the above is valid for:

$$(a/R_{\star})^2 \gg \frac{2}{3} \left(\frac{1+e}{1-e}\right)^3, \quad (35)$$

which may also be expressed in physical units as

$$\left(\frac{P}{\text{days}}\right)^{4/3} \gg 0.101 \left(\frac{\rho_{\star,\text{true}}}{\text{g cm}^{-3}}\right)^{-2/3} \left(\frac{1+e}{1-e}\right)^3. \quad (36)$$

As pointed out in numerous previous works (Burke 2008; Kipping 2008; Winn 2010; Dawson & Johnson 2012), if a planet on an eccentric orbit is observed to transit, then a-priori it is more probable that $0 < \omega \leq \pi$ than $\pi < \omega \leq 2\pi$. This is because the geometric transit probability is given by

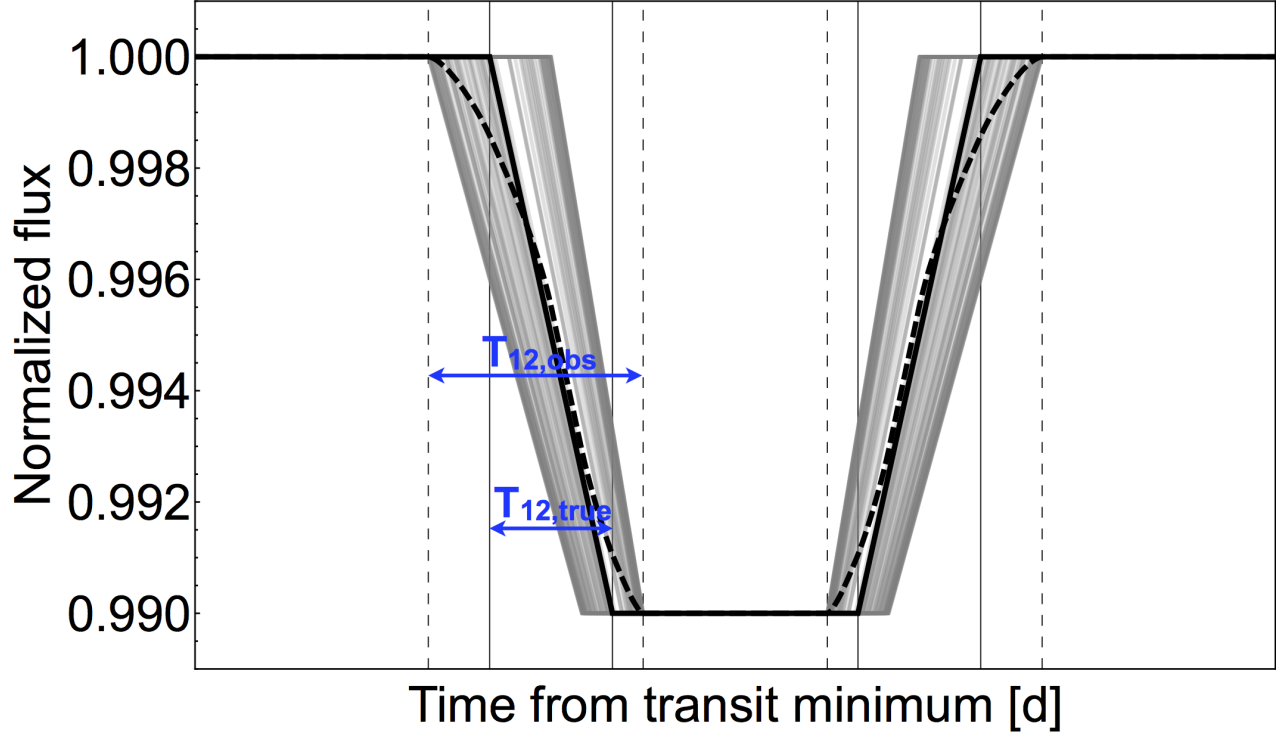


Figure 4. *The Photo-duration Effect:* If even low-amplitude transit duration variations (TDVs) are negated, a folded transit light curve will exhibit deformation leading to the erroneous retrieval of the basic transit parameters, including the observed stellar density, $\rho_{\star,\text{obs}}$. Here, the black line represents the true original signal, the gray lines are 100 examples of the signal with unaccounted for sinusoidal TDVs and the black-dashed line is the naively folded transit light curve, exhibiting sizable deformation.

$$P(b \leq 1) = \frac{1}{(a/R_\star)} \frac{1 + e \sin \omega}{1 - e^2} \quad (37)$$

and so

$$\frac{P(0 < \omega \leq \pi | b \leq 1)}{P(\pi < \omega \leq 2\pi | b \leq 1)} = \frac{\pi + 2e}{\pi - 2e} \quad (38)$$

which is greater than 1 for all $0 < e \leq 1$. Note that the exact ratio cannot be estimated without assuming some prior distribution for the eccentricity. The consequence of this is that $\Psi > 1$ is a more probable result than $\Psi < 1$ by the odds-ratio derived above, given that a planet is transiting and eccentric. This is an important result because it means eccentric orbits *tend* to overestimate $(\rho_{\star,\text{obs}}/\rho_{\star,\text{true}})$ whereas all of the previous effects discussed, except the photo-mass effect, underestimate the density. However, it is also worth noting that even for moderately high eccentricities of say $e \sim 0.5$, the odds-ratio quoted above is ~ 2 and thus although an overestimated density is more likely from the photo-eccentric effect, it is not dramatically so.

3.6.2 Minimum eccentricity

The photo-eccentric effect directly reveals Ψ , which is a function of both e and ω . Ideally, one wishes to obtain information on both e and ω in isolation, but purely from an information theory perspective it is obvious this ideal can never be truly realized, since we have one measurement and two unknowns. Progress can be made by considering the minimum eccentricity. In the Appendix C, we show that the *minimum* eccentricity can be derived in the case of SAP and provide a single-domain function for e_{\min} as

$$e_{\min} = \left(\frac{\left(\frac{\rho_{\star,\text{obs}}}{\rho_{\star,\text{true}}} \right)^{2/3} - 1}{\left(\frac{\rho_{\star,\text{obs}}}{\rho_{\star,\text{true}}} \right)^{2/3} + 1} \right) \mathbb{H}\left[\left(\frac{\rho_{\star,\text{obs}}}{\rho_{\star,\text{true}}} \right) - 1 \right] \\ + \left(\frac{\left(1 - \left(\frac{\rho_{\star,\text{obs}}}{\rho_{\star,\text{true}}} \right)^{2/3} \right) \left(1 - \left(\frac{\rho_{\star,\text{obs}}}{\rho_{\star,\text{true}}} \right)^{2/3} + \left(\frac{\rho_{\star,\text{obs}}}{\rho_{\star,\text{true}}} \right)^{4/3} \right)}{1 + \left(\frac{\rho_{\star,\text{obs}}}{\rho_{\star,\text{true}}} \right)^2} \right) \mathbb{H}\left[1 - \left(\frac{\rho_{\star,\text{obs}}}{\rho_{\star,\text{true}}} \right) \right], \quad (39)$$

where $\mathbb{H}[x]$ is the Heaviside Theta function. We note that previous authors have derived or discuss double-domain functions for e_{\min} such as Barnes (2007) and

Kane et al. (2012). The single-domain function presented here simply combines the two domains using Heaviside Theta functions and uses stellar density as the observable rather than durations. We also stress that e_{\min} is purely a function of $(\rho_{*,\text{obs}}/\rho_{*,\text{true}})$ and no other terms. It is therefore possible to analytically calculate the uncertainty on e_{\min} using quadrature:

$$\sigma_{e_{\min}} = \frac{4}{3} \left(\frac{\rho_{*,\text{obs}}}{\rho_{*,\text{true}}} \right)^{-1/3} \left(1 + \left(\frac{\rho_{*,\text{obs}}}{\rho_{*,\text{true}}} \right)^{2/3} \right)^{-2} \sigma_{\rho_{*,\text{obs}}/\rho_{*,\text{true}}}, \quad (40)$$

where $\sigma_{e_{\min}}$ and $\sigma_{\rho_{*,\text{obs}}/\rho_{*,\text{true}}}$ are the uncertainties on the minimum eccentricity and ratio of the observed to true stellar density respectively.

The simple e_{\min} function is visualized in Figure 5, where one can see the PE effect can induce AP deviations up to $\mathcal{O}[10^2]$. In this figure, we also over-plot Kepler Objects of Interest (KOIs) with asteroseismologically measured $\rho_{*,\text{true}}$ values from Huber et al. (2013). The $\rho_{*,\text{obs}}$ term is computed for each KOI using the MAST archival database¹ entries of (a/R_*) and P . In principle, objects on the left-hand side (LHS) may be blends (since one does not expect a high proportion of eccentric planets on this side) and objects on the right are genuinely eccentric KOIs (therefore assuming that the photo-timing, photo-duration, photo-spot and photo-mass effects are minor). However, we caution that the large number of multis on the LHS, suggesting false-positive blended systems, is highly inconsistent with the expected low false-positive rates of multi-planet systems (Lissauer et al. 2012). We therefore advocate independent checks of these $\rho_{*,\text{obs}}$ values before drawing any conclusions, which is outside the scope of this work.

3.6.3 Comparison to marginalization

Calculating the minimum eccentricity using Equation 39 is distinct from the strategy on the photo-eccentric effect by Dawson & Johnson (2012) and Dawson et al. (2012) who propose marginalizing over ω , much like a nuisance parameter. The major advantage over marginalizing over ω is that one naturally incorporates the geometric transit probability effect and derives a singular estimate for e . This is useful since e represents the most physically useful parameter with respect to formation/evolution models (Ford & Rasio 2008; Jurić & Tremaine 2008; Socrates et al. 2012; Dong et al. 2013).

However, there are several drawbacks of this approach compared to simply computing e_{\min} using Equation 39. Firstly, one can only achieve this feat by assuming an a-priori distribution for the eccentricity since the geometric transit probability is functionally dependent on both e and ω , as discussed earlier. Therefore, the derived e value is fundamentally dependent upon the

assumed prior distribution for e , which is somewhat circular logic. In practice, Dawson & Johnson (2012) found varying the priors on e imposes only small changes in the derived posterior distributions of e , yet this we predict that this is only likely true where the data overwhelms the priors such as the cases considered by Dawson & Johnson (2012) of highly eccentric systems causing $(\rho_{*,\text{obs}}/\rho_{*,\text{true}}) \gg 1$.

Secondly, the act of marginalizing over a parameter which has not been significantly constrained by the data fundamentally reduces the information content of the final determination. In other words, one makes the final determination fuzzier. In essence, the marginalization in e space is over $e_{\min} < e < 1$, since $e < 1$ for all bound orbits. Irrespective of any reasonable prior on e , this will cause the marginalized e value to lie somewhere inbetween these two extrema and lead to elevated error bars relative to e_{\min} to accommodate this marginalization. Systems with a high e_{\min} will therefore appear to provide relatively small errors on the marginalized e , purely because there is “less room” between e_{\min} and unity. An example of this is evident with the high e_{\min} system of HD 17156b reported in Dawson & Johnson (2012) ($e_{\min} \sim 0.6$) giving $e = 0.71^{+0.16}_{-0.09}$ whereas the $e_{\min} \sim 0$ system of Kepler-22b yields much broader uncertainties of $e = 0.13^{+0.36}_{-0.13}$ (Kipping et al. 2013), despite both being bright targets with asteroseismology and high-quality photometry. In general then, we advocate at least providing the community with both the constrained, prior-independent e_{\min} term in addition to the lossy, marginalized e .

Thirdly, the simple analytic form of our expression for e_{\min} makes it attractive for rapid calculation on hundreds/thousands of systems. Transits may be fitted en masse assuming a circular orbit and then e_{\min} is easily computed without any tacit assumption on the e distribution. An alternative but equivalent approach would be to compile a database of $T_{14,\text{obs}}$, $T_{23,\text{obs}}$ and δ_{obs} from which one can also proceed to compute e_{\min} . Additionally, provided one knows the uncertainties on $\rho_{*,\text{obs}}$ and $\rho_{*,\text{true}}$, then the uncertainty on e_{\min} is easily recovered in a single expression given by Equation 40, at least under the assumption of no other AP effects. We propose that this would be an advantageous strategy for upcoming transit survey missions, such as TESS.

3.7 False-Positives

Let us define a “false-positive” planetary candidate to be one which orbits a different star to that for which we have an independent measure of the stellar density. In such a case, then it should be obvious that the two density estimates need not agree and can be grossly different (see Sliski & Kipping 2014 for examples of such cases). The exact difference will depend upon the spectral types of the two stars and the flux ratios. In this scenario, we have no information on $\rho_{*,\text{true}}$, since the independent measure corresponds to a different star. We also know that the star hosting the transiting body must be heavily blended

¹ <http://archive.stsci.edu/kepler/koi/search.php>

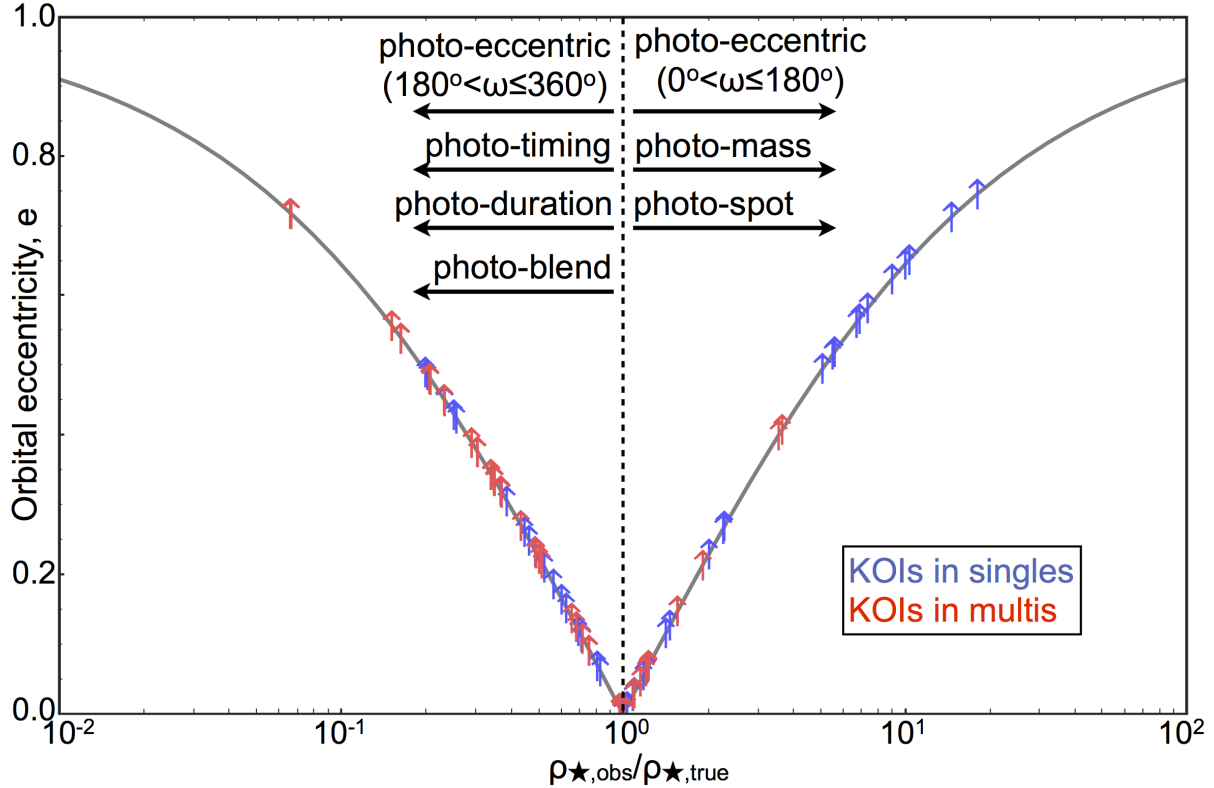


Figure 5. *The Photo-eccentric Effect:* The minimum orbital eccentricity function, defined in Equation 39, plotted with respect to its only dependent variable, $(\rho_{\star,\text{obs}}, \rho_{\star,\text{true}})$. The arrows correspond to real KOIs with known asteroseismology measurements available, where blue are singles and red are multis. We also mark the directions in which the other asterodensity profiling effects act.

and so the photo-blend effect must be acting. If we ignore the other AP effects, we may recall from Equation 14 that a limit exists on the maximum AP deviation due to the PB effect:

$$\left(\frac{\rho_{\star,\text{obs}}}{\rho_{\star,\text{true}}}\right) \geq \left(\frac{2p_{\text{obs}}(1 + \sqrt{1 - b_{\text{obs}}^2})}{(1 + p_{\text{obs}})^2 - b_{\text{obs}}^2}\right)^{3/2}. \quad (41)$$

This may be re-expressed to constrain the unknown quantity $\rho_{\star,\text{true}}$ via:

$$\rho_{\star,\text{alt}} \geq \rho_{\star,\text{obs}} \left(\frac{(1 + p_{\text{obs}})^2 - b_{\text{obs}}^2}{2p_{\text{obs}}(1 + \sqrt{1 - b_{\text{obs}}^2})}\right)^{3/2}, \quad (42)$$

where we replace $\rho_{\star,\text{true}}$ with $\rho_{\star,\text{alt}}$ to stress that the transiting body is orbiting an alternative star. We do not refer to this scenario as a “photo-name” effect, since unlike the other cases no independent information on the true stellar density is available. However, Equation 42, which is only valid in the absence of the PE, PT, PD, PM and PS effects, may be of use to observers vetting planetary candidates.

4 DISCUSSION

4.1 Consequences for Measuring Eccentricities with SAP

In this work, we have shown that at least five other asterodensity profiling effects exist in addition to the photo-eccentric effect, which are summarized in the “cheat sheet” of Figure 6. Since a number of phenomena can induce significant changes to the light curve derived stellar density, great care must be taken not to over-interpret any deviations as implying high eccentricity where none exists. Equivalently, one must be wary of interpreting a lack of significant discrepancies as implying most planets orbit on near-circular orbits. Put succinctly, the eccentricity distribution can only be extracted using AP with a careful consideration of the prior distributions for the other AP effects (e.g. the photo-blend effect, the photo-timing effect, etc). We would argue that any eccentricity distributions purported without such due diligence cannot be considered physically representative of the true sample. This statement is justified by the fact that not only are the other AP effects significant at the typical measurement uncertainties, but they will impart system-

atic shifts to any naively computed e distribution, since the parameters upon which they depend are often skewed in one direction (e.g. for the photo-blend effect the blend parameter must always be > 1 and thus always cause an underestimation of the stellar density).

Another important consequence of this work is that we find that the analytic model for the photo-eccentric effect is only valid under the condition that:

$$\left(\frac{P}{\text{days}}\right)^{4/3} \gg 0.101 \left(\frac{\rho_{\star,\text{true}}}{\text{g cm}^{-3}}\right)^{-2/3} \left(\frac{1+e}{1-e}\right)^3. \quad (43)$$

The above has a very steep dependency on e and rapidly rises as e approaches unity, due to the $(1-e)^{-3}$ term. This is particularly salient in light of the prediction and subsequent observational search for proto-hot Jupiters on super-eccentric orbits by Socrates et al. (2012) and Dawson et al. (2013) respectively. For example, if we wish to exploit the analytic photo-eccentric effect to search for objects with $e = 0.9$ around a Solar-like star then we require $P \gg 114$ days i.e. we need $P \gtrsim 1000$ d. If this condition is not satisfied, the highly eccentric planet would still induce a large $(\rho_{\star,\text{obs}}/\rho_{\star,\text{true}})$ discrepancy, but one cannot reliably use the photo-eccentric equations to back out e or e_{\min} .

For individual systems, priors on these other AP effects are likely less relevant since for many well-characterized transiting planet systems there are often additional observational constraints on many of the terms which affect the various AP effects e.g. rotational modulations, transit timing variations, adaptive optics, centroid offsets, etc. Therefore, SAP still presents arguably the most feasible technique for measuring the eccentricity of small, habitable-zone planets with current techniques (e.g. see the recent demonstration with the habitable-zone planet Kepler-22b, Kipping et al. 2013).

4.2 Blend analyses with MAP

Throughout this work we have derived analytic results for various AP effects in the Single-body Asterodensity Profiling (SAP) paradigm, since all results compare the observed stellar density to some independent ‘‘true’’ measure. However, it is trivial to extend our results to the case of Multi-body Asterodensity Profiling (MAP), which was first discussed in Kipping et al. (2012). By comparing the observed stellar density between transiting planets j and k , and assuming the objects orbit the same star, one is able to extract information on the state of a system. Since the issue of eccentricity is discussed in detail in Kipping et al. (2012), we do not repeat the arguments made in that work but briefly summarize that the authors found an analytic minimum constraint on the pair-wise sum of eccentricities for planets j and k is easily derived using MAP:

$$e_j + e_k \geq \frac{\Theta_{jk} - 1}{2}, \quad (44)$$

where

$$\Theta_{jk} \equiv \left(\frac{\rho_{\star,\text{obs},j}}{\rho_{\star,\text{obs},k}}\right)^{2/3}. \quad (45)$$

The two-thirds index was chosen since it naturally removes a three-halves index in the expression for the photo-eccentric effect. As shown in this work, it can be seen that the photo-blend effect also happens to be described by a three-halves power and thus the same Θ_{jk} definition is valuable in performing MAP for blend analysis. This is pertinent since the photo-blend effect can induce very large deviations in the observed stellar densities and, for heavily blended systems, this effect dominates AP. Using Equation 9 then, one may write the MAP blend equation as:

$$\Theta_{jk} = \frac{[(1 + \sqrt{\mathcal{B}} p_{\text{obs},j})^2 - b_{\text{obs},j}^2][(1 + p_{\text{obs},k})^2 - b_{\text{obs},k}^2]}{[(1 + \sqrt{\mathcal{B}} p_{\text{obs},k})^2 - b_{\text{obs},k}^2][(1 + p_{\text{obs},j})^2 - b_{\text{obs},j}^2]}. \quad (46)$$

It is possible to invert this equation and actually solving for $\sqrt{\mathcal{B}}$, yielding two roots from a quadratic equation:

$$\sqrt{\mathcal{B}_{\pm}^{\text{MAP}}} = \frac{p_{\text{obs},j} \alpha_{\text{obs},k} - \Theta_{jk} p_{\text{obs},k} \alpha_{\text{obs},j} \pm \sqrt{\mathcal{D}_{jk}}}{\Theta_{jk} p_{\text{obs},k}^2 \alpha_{\text{obs},j} - p_{\text{obs},j}^2 \alpha_{\text{obs},k}}, \quad (47)$$

where we make the substitutions

$$\alpha_k = (1 + p_{\text{obs},k})^2 - b_{\text{obs},k}^2, \quad (48)$$

$$\alpha_j = (1 + p_{\text{obs},j})^2 - b_{\text{obs},j}^2, \quad (49)$$

$$\begin{aligned} \mathcal{D}_{jk} = & b_{\text{obs},k}^2 p_{\text{obs},k} \alpha_{\text{obs},j}^2 \Theta_{jk}^2 - b_{\text{obs},j}^2 p_{\text{obs},j}^2 \alpha_{\text{obs},k}^2 \\ & - \alpha_{\text{obs},k} \alpha_{\text{obs},j} \Theta_{jk} \left[2p_{\text{obs},k} p_{\text{obs},j} \right. \\ & \left. - p_{\text{obs},k}^2 (1 - b_{\text{obs},j}^2) - p_{\text{obs},j}^2 (1 - b_{\text{obs},k}^2) \right]. \end{aligned} \quad (50)$$

As useful check of these expressions is to evaluate them in the limit of $\Theta_{jk} \rightarrow 1$, which would be the observed value in the absence of any blending:

$$\lim_{\Theta_{jk} \rightarrow 1} \sqrt{\mathcal{B}_{-}^{\text{MAP}}} = 1, \quad (51)$$

$$\begin{aligned} \lim_{\Theta_{jk} \rightarrow 1} \sqrt{\mathcal{B}_{+}^{\text{MAP}}} = & \left[p_{\text{obs},k} (2 + p_{\text{obs},k}) (1 - b_{\text{obs},j}^2) \right. \\ & \left. - p_{\text{obs},j} (2 + p_{\text{obs},j}) (1 - b_{\text{obs},k}^2) \right] \left[p_{\text{obs},j}^2 (1 - b_{\text{obs},k}^2) \right. \\ & \left. - p_{\text{obs},k}^2 (1 - b_{\text{obs},j}^2) + 2p_{\text{obs},k} p_{\text{obs},j} (p_{\text{obs},j} - p_{\text{obs},k}) \right]^{-1}. \end{aligned} \quad (52)$$

Therefore, as expected, we recover the $\mathcal{B} = 1$ solution corresponding to no blending. However, the second root cannot be trivially dismissed and is physically plausible. Generating uniform random values for $0 < p_{\text{obs},j} < 1$, $0 < p_{\text{obs},k} < 1$, $0 < b_{\text{obs},j} < (1 - p_{\text{obs},j})$

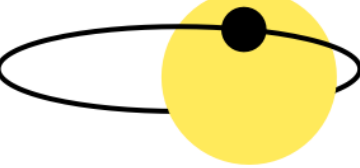
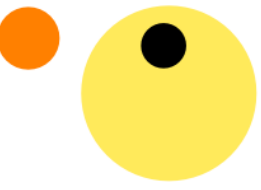
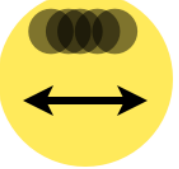
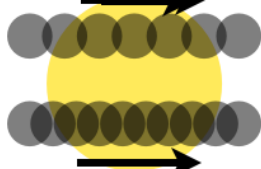
Photo-eccentric (PE) effect	$\lesssim 10^2$	
$\left(\frac{\rho_{\text{obs}}}{\rho_{\text{true}}}\right)^{\text{PE}} = \frac{(1 + e \sin \omega)^3}{(1 - e^2)^{3/2}}$ valid for: $\left(\frac{P}{\text{days}}\right)^{4/3} \gg 0.101 \left(\frac{\rho_{\star,\text{true}}}{\text{g cm}^{-3}}\right)^{-2/3} \left(\frac{1+e}{1-e}\right)^3$	$\lesssim 10^2$	
Photo-blend (PB) effect	$\lesssim 10^1$	
$\left(\frac{\rho_{\star,\text{obs}}}{\rho_{\star,\text{true}}}\right)^{\text{PB}} = \mathcal{B}^{-3/4} \left(\frac{(1 + \sqrt{\mathcal{B}} p_{\text{obs}})^2 - b_{\text{obs}}^2}{(1 + p_{\text{obs}})^2 - b_{\text{obs}}^2}\right)^{3/2}$ valid for: $\left(\frac{P}{\text{days}}\right)^{4/3} \gg 0.389 \left(\frac{\rho_{\star,\text{true}}}{\text{g cm}^3}\right)^{-2/3}$	$\lesssim 10^1$	
Photo-spot (PS) effect	$\lesssim 10^{-1}$	
$\left(\frac{\rho_{\star,\text{obs}}}{\rho_{\star,\text{true}}}\right)^{\text{PS}} = \lim_{\mathcal{B} \rightarrow \mathcal{B}_{\text{spot}}} \left(\frac{\rho_{\star,\text{obs}}}{\rho_{\star,\text{true}}}\right)^{\text{PB}}$ valid for: $\left(\frac{P}{\text{days}}\right)^{4/3} \gg 0.389 \left(\frac{\rho_{\star,\text{true}}}{\text{g cm}^3}\right)^{-2/3}$	$\lesssim 10^{-1}$	
Photo-timing (PT) effect	$\lesssim 10^0$	
$\left(\frac{\rho_{\star,\text{obs}}}{\rho_{\star,\text{true}}}\right)^{\text{PT}} \geq \left(\frac{p}{p + n A_{\text{TTV}}(a/R_{\star})}\right)^{3/2}$ valid for: $\left(\frac{P}{\text{days}}\right)^{4/3} \gg 0.231 \left(\frac{\rho_{\star,\text{true}}}{\text{g cm}^3}\right)^{-2/3}, 2A_{\text{TTV}} \ll T_{23}$	$\lesssim 10^0$	
Photo-duration (PD) effect	$\lesssim 10^0$	
$\left(\frac{\rho_{\star,\text{obs}}}{\rho_{\star,\text{true}}}\right)^{\text{PD}} = \left(\frac{(a/R_{\star})^2 p + 4A_{\text{TDV}}^2 b^2 p + 2A_{\text{TDV}}[(1-p^2)^2 - b^2(1+p^2)]}{(a/R_{\star})^2 [p + 4A_{\text{TDV}}^2 p + 2A_{\text{TDV}}(1+p^2-b^2)]}\right)^{3/2}$ valid for: $\left(\frac{P}{\text{days}}\right)^{4/3} \gg 0.231 \left(\frac{\rho_{\star,\text{true}}}{\text{g cm}^3}\right)^{-2/3}, A_{\text{TDV}} \ll 1$	$\lesssim 10^0$	
Photo-mass (PM) effect	$\lesssim 10^0$	
$\left(\frac{\rho_{\star,\text{obs}}}{\rho_{\star,\text{true}}}\right)^{\text{PM}} = 1 + \frac{M_{\text{transiter}}}{M_{\star}}$ always valid	$\lesssim 10^0$	

Figure 6. Asterodensity Profiling ‘‘Cheat Sheet’’: Summary of the analytic formulae for the various AP effects derived in this work, including the supported parameter range for their applicability. Red boxes provide approximate order-of-magnitude for each effect. All effects also assume $0 < b < (1 - p)$ i.e. a ‘‘flat-bottomed’’ transit.

and $0 < b_{\text{obs},k} < (1 - p_{\text{obs},k})$, we find that 68.3% of the samples lie in the range $1.4 < \mathcal{B}_+^{\text{MAP}} < 14.4$ with a median of 3.6. Therefore, in the limit of $\Theta_{jk} \rightarrow 1$, the $\mathcal{B}_+^{\text{MAP}}$ solution does not produce grossly large blend factors which can be easily dismissed as unphysical.

We therefore conclude that for 2-planet systems, blend analyses with MAP will be challenged by this apparent bi-modality. However, with $n \geq 3$ planets, one may derive $n!/(2!(n-2)!)$ pair-wise combinations of Θ_{jk} and the true solution for \mathcal{B} will be recovered in one of the two roots every time. Therefore, it should be possible to identify which root corresponds to the true solution in 3 or more planet solutions by root comparison. We leave more detailed investigations of MAP blend analysis to future studies.

4.3 Future Work

We hope that the investigations presented in this paper provide the foundational analytic theory for asterodensity profiling, but we are acutely aware that there is a great deal of theoretical and observational work still to accomplish in this new area of study. To begin with, there are numerous ignored effects known to distort the transit light curve and thus have the potential to impart AP signatures, such as planetary rings (Ohta et al. 2009; Barnes & Fortney 2004), planetary oblateness (Carter & Winn 2010), atmospheric lensing (Hui & Seager 2002), etc. We also did not consider cases where $p > 1$, such as total eclipses of white dwarfs discussed in Agol (2011).

In order to retrieve the eccentricity distribution using AP, we suggest that significant work is needed to understand the blend distribution, TTV distribution, starspot distribution, etc in order to adequately deconvolve the contribution from other AP effects. Well-characterized individual systems will likely be less dependent upon these prior distributions and so immediate observational progress can surely be made here (e.g. Dawson et al. 2012; Kipping et al. 2013). In such cases, we would advocate research into how well the blend factor can be constrained and whether systems can be practically validated using AP.

Despite these challenges, we envisage that AP can be a powerful tool for archival *Kepler* data and for the forthcoming TESS mission, for both measuring the eccentricity distribution and validating/vetting planetary candidates. This work also underscores the valuable symbiosis between exoplanet transits and asteroseismology for characterizing distant worlds.

ACKNOWLEDGMENTS

DMK would like to thank D. Sliski, S. Ballard and J. Irwin for very helpful conversations in the preparation of this work. Thanks to the anonymous reviewer for their constructive comments. DMK is supported by the NASA Sagan Fellowship.

REFERENCES

- Agol, E., 2011, ApJL, 731, 31
- Barnes, J. W. & Fortney, J. J., 2004, ApJ, 616, 1193
- Barnes, J. W., 2007, PASP, 119, 986
- Basri, G. et al., 2011, AJ, 141, 20
- Berdyugina, S. V., 2005, LRSP, 2, 8
- Burke, C. J. 2008, ApJ, 679, 1566
- Carter, J. A. & Winn, J. N., 2010, ApJ, 716, 850
- Carter, J. A., Winn, J. N., Holman, M. J., Fabrycky, D., Berta, Z. K., Burke, C. J. & Nutzman, P., 2011, ApJ, 730, 82
- Czesla, S., Huber, K. F., Wolter, U., Schröter, S. & Schmitt, J. H. M. M., 2009, A&A, 505, 1277
- Dawson, R. I. & Johnson, J. A., 2012, ApJ, 756, 13
- Dawson, R. I., Johnson, J. A., Morton, T. D., Crepp, J. R., Fabrycky, D. C., Murray-Clay, R. A. & Howard, A. W., 2012, ApJ, 761, 16
- Dawson, R. I., Murray-Clay, R. A. & Johnson, J. A. 2013, ApJ, submitted (astro-ph:1211.0554)
- Dong, S., Katz, B. & Socrates, A., 2013, ApJ, 763, 2
- Dressing, C. D., Spiegel, D. S., Scharf, C. A., Menou, K. & Raymond, S. N., 2010, ApJ, 721, 1295
- Ford, E. B. & Rasio, F. A. 2008, ApJ, 686, 621
- Ford, E. B. et al., 2012, ApJ, 756, 185
- Fressin, F. et al., 2011, ApJS, 197, 12
- Hartman, J. D., Bakos, G. Á. & Torres, G., 2011, “Detection and Dynamics of Transiting Exoplanets”, eds: F. Bouchy, R. Díaz & C. Moutou, Vol. 11, id. 02002
- Huber, D. et al., 2013, ApJ, 767, 17
- Hui, L. & Seager, S., 2002, ApJ, 572, 540
- Jurić, M. & Tremaine, S., 2008, ApJ, 686, 603
- Kane, S. R., Ciardi, D. R., Gelino, D. M. & von Braun, K., 2012, MNRAS, 425, 757
- Kipping, D. M., 2008, MNRAS, 389, 1383
- Kipping, D. M. & Tinetti, G., 2012, MNRAS, 407, 2589
- Kipping, D. M., 2009a, MNRAS, 392, 181
- Kipping, D. M., 2009b, MNRAS, 396, 1797
- Kipping, D. M. 2010a, MNRAS, 407, 301
- Kipping, D. M., 2010b, MNRAS, 408, 1758
- Kipping, D. M. & Tinetti, G., 2010, MNRAS, 407, 2589
- Kipping, D. M., Dunn, W. R., Jasinski, J. M. & Manthri, V. M., 2012, MNRAS, 421, 1166
- Kipping, D. M., 2012, MNRAS, 427, 2487
- Kipping, D. M., Forgan, D., Hartman, J., Nesvorný, D., Bakos, G. Á., Schmitt, A. R. & Buchhave, L. A., 2013, ApJ, 777, 134
- Kipping, D. M., 2012, MNRAS, 435, 2152
- Lissauer, J. J. et al., 2012, ApJ, 750, 112
- Mandel, K. & Agol, E., 2002, ApJ, 580, 171
- Mazeh, T. et al., 2013, ApJS, 208, 16
- Moorhead, A. V. et al., 2011, ApJS, 197, 1
- Morton, T. D. & Johnson, J. A., 2011, ApJ, 738, 170
- Nesvorný, D., Kipping, D. M., Buchhave, L. A., Bakos, G. Á., Hartman, J. & Schmitt, A. R., 2012, Science, 336, 1133
- Ohta, Y., Taruya, A. & Suto, Y., 2009, ApJ, 690, 1
- Sanchis-Ojeda, R., Rappaport, S., Winn, J. N., Levine, A., Kotson, M. C., Latham, D. W. & Buchhave, L. A.,

- 2013, ApJ, 774, 54
Seager, S. & Mallén-Ornelas, G., 2003, ApJ, 585, 1038
Sliski, D. H. & Kipping, D. M., 2014, ApJ, submitted
(astro-ph:1401.1207)
Socrates, A., Katz, B., Dong, S. & Tremaine, S. 2012,
ApJ, 750, 106
Sozzetti, A., Torres, G., Charbonneau, D., Latham,
D. W., Holman, M. J., Winn, J. N., Laird, J. B. &
O'Donovan, F. T., 2007, ApJ, 664, 1190
Torres, G. et al., 2011, ApJ, 727, 24
Ulrich, R. K., 1986, ApJ, 306, 37
Walkowicz, L. M. & Basri, G. S., 2013, MNRAS, In
Press
Winn, J. N., 2010, *Transits and Occultations*, EXO-
PLANETS, University of Arizona Press; ed: S. Seager

APPENDIX A: DERIVATION OF THE PHOTO-BLEND EFFECT

A1 Ratio-of-radii bias

We here provide a formal derivation for the photo-blend effect, followed by in subsequent appendices by other relevant derivations of important results presented in this paper. All derivations, unless otherwise stated, will follow the methodology outlined in §2.3. Further, for each derivation of a specific AP effect, all other AP effects will be ignored in order to provide results for each effect in isolation.

We begin by considering blends. By virtue of the definition of the blend factor given in Equation 8, the transit depth of a blended source will be diminished by the factor \mathcal{B} . It therefore follows that the derived ratio-of-radii, p , is affected via

$$p_{\text{obs}} = p_{\text{true}} / \sqrt{\mathcal{B}}, \quad (\text{A1})$$

where we use the subscripts “true” and “obs” to distinguish between the truth and that which one naively adopts the standard simple assumptions of no blend, a circular orbit, etc. The true value may be therefore be retrieved using

$$p_{\text{true}} = p_{\text{obs}} \sqrt{\mathcal{B}}. \quad (\text{A2})$$

A2 Impact parameter bias

As stated earlier, we will ignore all other AP effects in what follows. Accordingly, one may define the transit impact parameter as a function of just three terms T_{14} , T_{23} and p , as demonstrated by Seager & Mallén-Ornelas (2003). In this framework, T_{14} is the first-to-fourth contact duration and T_{23} is the second-to-third contact duration. Critically, these durations are unaffected by the act of a blend (Kipping & Tinetti 2010). The same statement can also be said of the orbital period which is calculated by the interval between transits:

$$\begin{aligned} T_{14,\text{obs}} &= T_{14,\text{true}} = T_{14}, \\ T_{23,\text{obs}} &= T_{23,\text{true}} = T_{23}, \\ P_{\text{obs}} &= P_{\text{true}} = P, \end{aligned} \quad (\text{A3})$$

where we drop the explicit “true” subscript on the right-hand side (RHS). We follow this pattern in what follows, where the reader should interpret any term missing an explicit true/obs subscript to imply that we are referring to the true value. Having now defined the effect of blends on each of the key observable terms, we may now feed our expressions for p_{obs} , $T_{14,\text{obs}}$ and $T_{23,\text{obs}}$ into Equation 2 from Seager & Mallén-Ornelas (2003) to derive the observed impact parameter:

$$b_{\text{obs}}^2 = \frac{(1 - p_{\text{true}} \mathcal{B}^{-1/2})^2 - \frac{\sin^2(T_{23}\pi/P)}{\sin^2(T_{14}\pi/P)}(1 + p_{\text{true}} \mathcal{B}^{-1/2})^2}{1 - \frac{\sin^2(T_{23}\pi/P)}{\sin^2(T_{14}\pi/P)}}. \quad (\text{A4})$$

Let us assume that $\mathcal{B} = 1$ i.e. no blend is present. Plugging equations Equation 1 into Equation A4 in this limit yields

$$\lim_{\mathcal{B} \rightarrow 1} b_{\text{obs}}^2 = b_{\text{true}}^2, \quad (\text{A5})$$

as expected. Now consider that a blend source is present. Again feeding Equation 1 Equation A4 yields (without any approximation):

$$b_{\text{obs}}^2 = \frac{\mathcal{B} + p_{\text{true}}^2 - \sqrt{\mathcal{B}}(1 + p_{\text{true}}^2 - b_{\text{true}}^2)}{\mathcal{B}}. \quad (\text{A6})$$

Since the above expression clearly scales with b_{true} , then we may find the maximum/minimum range of the above by evaluating when $b_{\text{true}} \rightarrow b_{\text{true,min}} = 0$ and $b_{\text{true}} \rightarrow b_{\text{true,max}} = 1 - p_{\text{true}}$:

$$\frac{\mathcal{B} + p_{\text{true}}^2}{\mathcal{B}} - \frac{1 + p_{\text{true}}^2}{\sqrt{\mathcal{B}}} \leq b_{\text{obs}}^2 \leq \frac{\mathcal{B} + p_{\text{true}}^2}{\mathcal{B}} - \frac{2p_{\text{true}}}{\sqrt{\mathcal{B}}} \quad (\text{A7})$$

If we replace p_{true} with $p_{\text{obs}}\sqrt{\mathcal{B}}$ then the RHS simplifies to $b_{\text{obs}} \leq (1 - p_{\text{obs}})$, displaying an analogous form the the boundary condition imparted on the true impact parameter. In the limit of no blending and extreme blending, Equation A7 gives:

$$\begin{aligned} 0 \leq \lim_{\mathcal{B} \rightarrow 1} b_{\text{obs}}^2 &\leq (1 - p_{\text{true}})^2 \\ 1 \leq \lim_{\mathcal{B} \rightarrow \infty} b_{\text{obs}}^2 &\leq 1. \end{aligned} \quad (\text{A8})$$

Therefore, we find that $0 \leq b_{\text{obs}} \leq (1 - p_{\text{true}})$. Recall that we have also showed that $0 \leq b_{\text{obs}} \leq (1 - p_{\text{obs}})$. Since both statements are true, one must take precedent over the other and since $p_{\text{obs}} < p_{\text{true}}$ then the latter limit is the more constraining one i.e. $0 \leq b_{\text{obs}} \leq (1 - p_{\text{obs}})$ for all $\mathcal{B} \geq 1$ and $0 \leq b_{\text{true}} \leq (1 - p_{\text{true}})$.

Equation A6 may be re-written by replacing the p_{true} terms with the observed values to give

$$b_{\text{obs}}^2 = 1 + p_{\text{obs}}^2 - \left(\frac{1 + \mathcal{B}p_{\text{obs}}^2 - b_{\text{true}}^2}{\sqrt{\mathcal{B}}} \right). \quad (\text{A9})$$

The inverse of this expression is easily shown to be:

$$b_{\text{true}}^2 = 1 + \mathcal{B}p_{\text{obs}}^2 - \sqrt{\mathcal{B}}(1 - b_{\text{obs}}^2) - p_{\text{obs}}^2. \quad (\text{A10})$$

A3 Scaled semi-major axis bias

The scaled semi-major axis, (a/R_*) , can also be derived from the observed durations and ratio-of-radii via Equation 3, to give:

$$(a/R_\star)^2_{\text{obs}} = \frac{(1+p_{\text{obs}})^2 - b_{\text{obs}}^2(1 - \sin^2(T_{14}\pi/P))}{\sin^2(T_{14}\pi/P)}. \quad (\text{A11})$$

In the limit of no blend, then $b_{\text{obs}} \rightarrow b_{\text{true}}$ and $p_{\text{obs}} \rightarrow p_{\text{true}}$, giving the expected result that

$$\lim_{B \rightarrow 1} (a/R_\star)^2_{\text{obs}} = (a/R_\star)^2_{\text{true}}. \quad (\text{A12})$$

However, in the case of a non-unity blend factor, we find

$$(a/R_\star)^2_{\text{obs}} = \left(\frac{(a/R_\star)^2 - b^2}{(1+p)^2 - b^2} \right) \left((1+p)^2 - \frac{[(a/R_\star)^2 - (1+p)^2][B + p^2 - \sqrt{B}(1+p^2 - b^2)]}{B[(a/R_\star)^2 - b^2]} \right). \quad (\text{A13})$$

A4 Mean stellar density bias

Finally, we come to the parameter of interest, the mean stellar density, $\rho_{\star,\text{obs}}$. Following the definition in Equation 4, we have:

$$\rho_{\star,\text{obs}} \equiv \frac{3\pi(a/R_\star)^{3/2}_{\text{obs}}}{GP^2}. \quad (\text{A14})$$

As before, for an unblended target star we recover

$$\lim_{B \rightarrow 1} \rho_{\star,\text{obs}} = \rho_{\star,\text{true}}. \quad (\text{A15})$$

For blended planets, the equation is more complicated, particular when we make the substitution that $(a/R_\star)^3_{\text{true}} = (GP^2\rho_{\star,\text{true}})/(3\pi)$.

By inspection of Equation A13, we found that assuming $(a/R_\star)^2 \gg (1+p)^2$ (which also imparts $(a/R_\star)^2 \gg b^2$ since $b < (1+p)$ in order for a transit to occur) allows for significant reduction in the form of the expression for $(\rho_{\star,\text{obs}}/\rho_{\star,\text{true}})$ to:

$$\lim_{(a/R_\star)^2 \gg (1+p)^2} \left(\frac{\rho_{\star,\text{obs}}}{\rho_{\star,\text{true}}} \right) = \left(\frac{(1+p)^2 - b_{\text{obs}}^2}{(1+p)^2 - b^2} \right)^{3/2} \quad (\text{A16})$$

Since we assume that the transit displays a flat bottom, then $b^2 \lesssim 1$ and $p \lesssim 1$ giving us $(1+p)^2 \lesssim 4$ so that our assumption becomes $(a/R_\star)^2 \gg 4$. By definition, $(a/R_\star) > 1$ at all times in order for the transit to be physical (otherwise the transiting object is inside the star). Whilst the majority of exoplanets easily satisfy the condition that $(a/R_\star)^2 \gg 4$, some very short-period objects such as Kepler-78b have $(a/R_\star)^2 \sim 3$ (Sanchis-Ojeda et al. 2013). (a/R_\star) may be estimated using P and $\rho_{\star,\text{true}}$ and converting into typical units of measure we determine that our approximation is valid for:

$$\left(\frac{P}{\text{days}} \right)^{4/3} \gg 0.389 \left(\frac{\rho_{\star,\text{true}}}{\text{g cm}^3} \right)^{-2/3} \quad (\text{A17})$$

Under this condition then, one may re-write Equation A16 in terms of the observables:

$$\lim_{(a/R_\star)^2 \gg (1+p)^2} \left(\frac{\rho_{\star,\text{obs}}}{\rho_{\star,\text{true}}} \right) = \left(\frac{(1 + \sqrt{B}p_{\text{obs}})^2 - b_{\text{obs}}^2}{\sqrt{B}((1 + p_{\text{obs}})^2 - b_{\text{obs}}^2)} \right)^{3/2}. \quad (\text{A18})$$

A5 Solving for the blend parameter

Since the observer directly determines p_{obs} and b_{obs} , then Equation A18 suggests that one should be able to invert the above and infer B . However, in doing so, we find that one recovers a quadratic solution and both roots are ostensibly plausible:

$$\begin{aligned} \mathcal{B}_{+,-} = & \frac{1}{4p_{\text{obs}}^4} \left(-2p_{\text{obs}} + \left(\frac{\rho_{\star,\text{obs}}}{\rho_{\star,\text{true}}} \right)^{2/3} [(1 + p_{\text{obs}})^2 - b_{\text{obs}}^2] \right. \\ & \pm \left[\left(p_{\text{obs}} \left[(2 + p_{\text{obs}}) \left(\frac{\rho_{\star,\text{obs}}}{\rho_{\star,\text{true}}} \right)^{2/3} - 2 \right] \right. \right. \\ & \left. \left. + \left(\frac{\rho_{\star,\text{obs}}}{\rho_{\star,\text{true}}} \right)^{2/3} (1 - b_{\text{obs}}^2) \right)^2 - 4p_{\text{obs}}^2(1 - b_{\text{obs}}^2) \right]^{1/2} \right) \end{aligned} \quad (\text{A19})$$

There are several analytic insights that can be made with this expression. Firstly, at the extreme solution of $(\rho_{\star,\text{obs}}/\rho_{\star,\text{true}}) = 1$, example plots of the functions (e.g. see Figure 1) show that these points correspond to the maximum and minimum in \mathcal{B} -space:

$$\mathcal{B} \geq \lim_{(\rho_{\star,\text{obs}}/\rho_{\star,\text{true}}) \rightarrow 1} \mathcal{B}_- = 1, \quad (\text{A20})$$

$$\mathcal{B} \leq \lim_{(\rho_{\star,\text{obs}}/\rho_{\star,\text{true}}) \rightarrow 1} \mathcal{B}_+ = \frac{(1 - b_{\text{obs}}^2)^2}{p_{\text{obs}}^4}. \quad (\text{A21})$$

We also note that two functions, \mathcal{B}_+ and \mathcal{B}_- , meet at an apparent minimum in $(\rho_{\star,\text{obs}}/\rho_{\star,\text{true}})$ -space. This point is found by solving $\partial(\rho_{\star,\text{obs}}/\rho_{\star,\text{true}})/\partial B = 0$ for B , giving:

$$\lim_{\left(\frac{\rho_{\star,\text{obs}}}{\rho_{\star,\text{true}}} \right) \rightarrow \left(\frac{\rho_{\star,\text{obs}}}{\rho_{\star,\text{true}}} \right)_{\min}} \mathcal{B} = \frac{1 - b_{\text{obs}}^2}{p_{\text{obs}}^2}, \quad (\text{A22})$$

which may be used to determine the equivalent location in $(\rho_{\star,\text{obs}}/\rho_{\star,\text{true}})$ -space, corresponding to the maximum and minimum limits of said parameter:

$$\left(\frac{\rho_{\star,\text{obs}}}{\rho_{\star,\text{true}}} \right) \geq \left(\frac{\rho_{\star,\text{obs}}}{\rho_{\star,\text{true}}} \right)_{\min} = \left(\frac{2p_{\text{obs}}(1 + \sqrt{1 - b_{\text{obs}}^2})}{(1 + p_{\text{obs}})^2 - b_{\text{obs}}^2} \right)^{3/2}, \quad (\text{A23})$$

$$\left(\frac{\rho_{\star,\text{obs}}}{\rho_{\star,\text{true}}} \right) \leq \left(\frac{\rho_{\star,\text{obs}}}{\rho_{\star,\text{true}}} \right)_{\max} = 1. \quad (\text{A24})$$

Crucially then, a measurement of $(\rho_{*,\text{obs}}/\rho_{*,\text{true}})$ below the minimum or above the maximum should not be possible for any degree of blending. Such a case therefore would mean that another AP effect is responsible for the deviation (which realistically can only be the photo-eccentric effect) or the star hosting the eclipsing body does not possess a true stellar density equal to $\rho_{*,\text{true}}$.

Finally, we note that the contours never cross the small-planet limit found by evaluating Equation A18 in the limit $p_{\text{obs}} \ll 1$:

$$\lim_{p_{\text{obs}} \ll 1} \left(\lim_{(a/R_*)^2 \gg (1+p)^2} \left(\frac{\rho_{*,\text{obs}}}{\rho_{*,\text{true}}} \right) \right) = \mathcal{B}^{-3/4}. \quad (\text{A25})$$

A6 Allowed Range of \mathcal{B}_-

Plotting some example functions in Figure 1 reveals that the \mathcal{B}_+ solutions extend up to suspiciously high \mathcal{B} . This issue can be phrased mathematically by computing the true value of p once one corrects for the blending factor, given by Equation A2. Since a fundamental assumption of our work is that a flat-bottomed transit is observed, then we expect $p_{\text{true}} < (1 - b_{\text{true}})$ at all times and since the minimum value of b_{true} is zero then the maximum limit is $p_{\text{true}} < 1$. By this criteria and inspection of the contours in Figure 1, we note that there appear to be some apparently forbidden p_{true} values along the \mathcal{B}_+ contour with \mathcal{B} reaching $\sim 10^8$.

Before exploring the very high blend factors produced by the \mathcal{B}_+ root, we first evaluate the maximum possible p_{true} value along the \mathcal{B}_- contour, which occurs at the point where the \mathcal{B}_- meets \mathcal{B}_+ i.e. when $(\rho_{*,\text{obs}}/\rho_{*,\text{true}}) \rightarrow (\rho_{*,\text{obs}}/\rho_{*,\text{true}})_{\min}$:

$$\lim_{(\rho_{*,\text{obs}}/\rho_{*,\text{true}}) \rightarrow (\rho_{*,\text{obs}}/\rho_{*,\text{true}})_{\min}} p_{\text{true}} = \sqrt{1 - b_{\text{obs}}^2} \quad (\text{A26})$$

We have already derived an expression for b_{obs} earlier in Equation A9, which scales with b_{true} . It was shown earlier than $0 \leq b_{\text{obs}} \leq (1 - p_{\text{obs}})$ for the allowed parameter range considered in this study. This means that $p_{\text{true}} < \sqrt{1 - (1 - p_{\text{obs}})^2} \leq 1$ since $p_{\text{obs}} \leq 1$. This therefore proves that all loci along the \mathcal{B}_- contour reside in unforbidden parameter space.

A7 Allowed Range of \mathcal{B}_+

It is easy to show that at least some of the loci along the \mathcal{B}_+ contour produce $p_{\text{true}} > 1$ and thus break the fundamental assumptions of our work. For example, consider the maximum possible of \mathcal{B}_+ found when $(\rho_{*,\text{obs}}/\rho_{*,\text{true}}) \rightarrow 1$, as mentioned earlier:

$$\lim_{(\rho_{*,\text{obs}}/\rho_{*,\text{true}}) \rightarrow 1} \mathcal{B}_+ = \frac{(1 - b_{\text{obs}}^2)^2}{p_{\text{obs}}^4}. \quad (\text{A27})$$

Requiring $p_{\text{true}} < 1$ is equivalent to $\mathcal{B} < p_{\text{obs}}^{-2}$ which means that in order for the above satisfy this we require

$(1 - b_{\text{obs}}^2) < p_{\text{obs}}$. However, since $b_{\text{obs}} < 1 - p_{\text{obs}}$ as shown earlier in Appendix A2, then this condition can *never* be in effect. Therefore, there is no doubt that \mathcal{B}_+ at least partially samples forbidden parameter space.

We may actually solve for the point along \mathcal{B}_+ when this breakdown occurs. This must occurs when $\mathcal{B}_+ = p_{\text{obs}}^{-2}$ since we require $p_{\text{true}} < 1$ which implies $\mathcal{B} < p_{\text{obs}}^{-2}$ at all times. Solving this expression for $(\rho_{*,\text{obs}}/\rho_{*,\text{true}})$ yields a quadratic equation with two roots. The first root has the solution:

$$\left(\frac{\rho_{*,\text{obs}}}{\rho_{*,\text{true}}} \right) = \left(\frac{b_{\text{obs}}^2 p_{\text{obs}}}{(1 + p_{\text{obs}})^2 - b_{\text{obs}}^2} \right)^{3/2}. \quad (\text{A28})$$

This may be compared to the minimum allowed value of $(\rho_{*,\text{obs}}/\rho_{*,\text{true}})$ derived earlier in Equation A24, meaning that we require:

$$\begin{aligned} \left(\frac{b_{\text{obs}}^2 p_{\text{obs}}}{(1 + p_{\text{obs}})^2 - b_{\text{obs}}^2} \right)^{3/2} &> \left(\frac{2p_{\text{obs}}(1 + \sqrt{1 - b_{\text{obs}}^2})}{(1 + p_{\text{obs}})^2 - b_{\text{obs}}^2} \right)^{3/2}, \\ \Rightarrow b_{\text{obs}}^2 &\not> 2(1 + \sqrt{1 - b_{\text{obs}}^2}) \quad \forall 0 < b_{\text{obs}} < 1 \end{aligned} \quad (\text{A29})$$

where the second line shows the condition is not satisfied (in fact the exact opposite condition is in effect). This allows us to summarily reject this root as a genuine solution. The remaining root has the form:

$$\left(\frac{\rho_{*,\text{obs}}}{\rho_{*,\text{true}}} \right)_{\mathcal{B}_{+,\max}} = \left(\frac{(4 - b_{\text{obs}}^2)p_{\text{obs}}}{(1 + p_{\text{obs}})^2 - b_{\text{obs}}^2} \right)^{3/2}, \quad (\text{A30})$$

which does satisfy the condition of being greater than the minimum estimate in Equation A24 for all $b_{\text{obs}} > 0$. This maximum limit is marked with gray circles on the example plots shown in Figure 1. Therefore, \mathcal{B}_+ produces is a valid solution when we have:

$$\left(\frac{\rho_{*,\text{obs}}}{\rho_{*,\text{true}}} \right)_{\min} < \left(\frac{\rho_{*,\text{obs}}}{\rho_{*,\text{true}}} \right) < \left(\frac{\rho_{*,\text{obs}}}{\rho_{*,\text{true}}} \right)_{\mathcal{B}_{+,\text{crit}}}. \quad (\text{A31})$$

A measurement of the density in this range means that the inverse solution for \mathcal{B} has two roots. Therefore, one should expect a bi-modal posterior distribution for \mathcal{B} when using SAP in such cases, provided the prior range in \mathcal{B} is allowed to explore to high blend factors. We also note that in the the limit of $b_{\text{obs}}^2 \rightarrow 0$ then $(\rho_{*,\text{obs}}/\rho_{*,\text{true}})_{\min} = (\rho_{*,\text{obs}}/\rho_{*,\text{true}})_{\mathcal{B}_{+,\text{crit}}}$ meaning the \mathcal{B}_+ solution is always forbidden in such a case. This is also evident in the top-left panel of Figure 1 where the two curves corresponding to these limits overlap.

APPENDIX B: VALID RANGE FOR THE ANALYTIC PHOTO-ECCENTRIC EFFECT

B1 The Transit Duration Equation

In this paper, we assume that the observed stellar density is affected by the photo-eccentric effect via a simple analytic formula. In this section, we investigate under what

conditions this simple formula is actually a valid since there appears to be no previous efforts to quantify the validity of this crucial assumption. The observed stellar density is assumed to behave as (Kipping 2010a):

$$\left(\frac{\rho_{*,\text{obs}}}{\rho_{*,\text{true}}}\right) = \Psi, \quad (\text{B1})$$

where we define

$$\Psi \equiv \frac{(1 - e \sin \omega)^3}{(1 - e^2)^{3/2}}. \quad (\text{B2})$$

Inferences about the eccentricity of a system made using the above expressions are defined here as exploiting the analytic photo-eccentric. These expressions are taken from Kipping (2010a) but we note that many other authors have used this function for modeling the photo-eccentric effect (Winn 2010; Carter 2011; Kipping et al. 2012; Dawson & Johnson 2012). Given the widespread use of this expression, it is crucial to understand the limits of the equation in question. The expressions above are derived by setting $T_{14,\text{obs}}$ and $T_{23,\text{obs}}$ to that expected for a planet with orbital eccentricity, e , and argument of periastron, ω . To date, there is no known exact analytic expression for the duration of a transit on an eccentric orbit but Kipping (2010a) derived an approximate expression, provided by Equation 15 of that work:

$$T_{14}^{23} = \frac{P}{\pi} \frac{\varrho_c^2}{\sqrt{1-e^2}} \sin^{-1} \sqrt{\frac{(1 \pm p)^2 - b^2}{(a/R_*)^2 \varrho_c^2 - b^2}}, \quad (\text{B3})$$

where Kipping (2010a) define

$$\varrho_c \equiv \frac{1 - e^2}{1 + e \sin \omega}. \quad (\text{B4})$$

Kipping (2010a) demonstrate that Equation B3 is an excellent approximation to the true transit duration (which can be computed more laboriously via the method described in Kipping 2008). As demonstrated in Kipping (2010a), these approximate expressions become most erroneous when (a/R_*) is small. However, even at $(a/R_*) = 5$, the expression performs better than 1% accuracy across the vast majority of parameter space and the paper finds an impressive average accuracy of $< 0.1\%$ for $|e \sin \omega| < 0.5$ and $|e \cos \omega| < 0.85$. Compared to the other assumptions made in deriving Equation B1, which we will shortly discuss, Equation B3 is unlikely to ever be the bottleneck in accuracy.

Although Kipping (2010a) spent great effort exploring the accuracy of Equation B3, no effort is spent on the accuracy of the most relevant equation for the analytic photo-eccentric effect i.e. Equation B1. The reason for this is quite simply that the photo-eccentric effect had not been envisaged at this time and so the importance of Equation B1 was not realized. Therefore, we devote this section to addressing this important question.

B2 Accuracy of the Impact Parameter Approximation

As with other asterodensity effects, not only is $(a/R_*)_{\text{obs}}$ (and thus $\rho_{*,\text{obs}}$) deviant from the truth, but also the observed impact parameter, b_{obs} , is deviant. Using Equation B3 and the original Seager & Mallén-Ornelas (2003) equations, Kipping (2010a) (see Equation 33) showed that (without any approximations):

$$b_{\text{obs}}^2 = 1 + p^2 + 2p \left(\frac{\sin^2 \left[\frac{\varrho_c^2}{\sqrt{1-e^2}} \sin^{-1} \left(\frac{\sqrt{(1-p)^2 - b^2}}{a R_* \varrho_c \sin i} \right) \right] + \sin^2 \left[\frac{\varrho_c^2}{\sqrt{1-e^2}} \sin^{-1} \left(\frac{\sqrt{(1+p)^2 - b^2}}{a R_* \varrho_c \sin i} \right) \right]}{\sin^2 \left[\frac{\varrho_c^2}{\sqrt{1-e^2}} \sin^{-1} \left(\frac{\sqrt{(1-p)^2 - b^2}}{a R_* \varrho_c \sin i} \right) \right] - \sin^2 \left[\frac{\varrho_c^2}{\sqrt{1-e^2}} \sin^{-1} \left(\frac{\sqrt{(1+p)^2 - b^2}}{a R_* \varrho_c \sin i} \right) \right]} \right). \quad (\text{B5})$$

Kipping (2010a) briefly remark that making a small-angle approximation in the trigonometric functions allows one to simplify the above to $b_{\text{obs}}^2 = b^2$. However, what remains unclear is exactly under what conditions is a small-angle approximation valid? The small-angle approximation is actually implemented four times in total, two of which correspond to $\sin^{-1} x \simeq x$ and two of which correspond to $\sin x \simeq x$. Let us begin by inspecting the validity of the inverse sine approximation.

B2.1 Accuracy of the inverse sine small-angle approximation

The inverse sine approximation in question is fully expressed as:

$$\sin^{-1} \sqrt{\frac{(1 \pm p)^2 - b^2}{(a/R_*)^2 \varrho_c^2 - b^2}} \simeq \sqrt{\frac{(1 \pm p)^2 - b^2}{(a/R_*)^2 \varrho_c^2 - b^2}}. \quad (\text{B6})$$

It is trivial to show that the ϱ_c term has two extrema at $\omega = \pi/2$ and $\omega = 3\pi/2$ and so we may consider four distinct cases under which we require the above approximation to remain true:

- [1] $(1 \pm p) \rightarrow (1 + p)$ and $\varrho_c \rightarrow \lim_{\omega \rightarrow \pi/2} \varrho_c$
- [2] $(1 \pm p) \rightarrow (1 + p)$ and $\varrho_c \rightarrow \lim_{\omega \rightarrow 3\pi/2} \varrho_c$
- [3] $(1 \pm p) \rightarrow (1 - p)$ and $\varrho_c \rightarrow \lim_{\omega \rightarrow \pi/2} \varrho_c$
- [4] $(1 \pm p) \rightarrow (1 - p)$ and $\varrho_c \rightarrow \lim_{\omega \rightarrow 3\pi/2} \varrho_c$

In each case, the remaining variables are (a/R_*) , b , e and p . Let us proceed by finding the maximum of the inverse sine function's argument in all four cases. We demonstrate this by Monte Carlo experiment where we draw random uniform variates for $0 < p < 1$, $0 < b < (1-p)$ and $0 < e < e_{\text{max}}$. For each realization, we plot the inverse sine argument as a function of the only remaining dependent variable, (a/R_*) . We make 1000 plots for each of the four cases and in each case we determine the maximum value of the inverse sine function's argument, with respect to (a/R_*) and e_{max} . In practice

this is done by both varying the experiments for several different e_{\max} values and taking the derivatives of the inverse sine function's argument. In all Monte Carlo experiments, we enforce the condition that $(a/R_*) > (1-e)$ to avoid the planet colliding into the star. Figure B1 displays our results when we arbitrarily choose $e_{\max} = 0.5$.

After conducting this analysis, for which some results are illustrated in Figure B1, we are able to derive functional upper limits on the the inverse sine function's argument with respect to (a/R_*) and e_{\max} . From these four maxima functions, one may use the maximum of *these* to demonstrate that:

$$\sqrt{\frac{(1 \pm p)^2 - b^2}{(a/R_*)^2 \varrho_c^2 - b^2}} \leq \frac{2}{(a/R_*)(1-e)} \\ \forall (0 \leq p < 1); (0 \leq b < 1-p); (0 \leq \omega < 2\pi); (0 \leq e < 1). \quad (\text{B7})$$

Armed with the above, one may now answer the question as to what range of orbits the small-angle inverse sine approximation is valid. The Maclaurin series expansion of the inverse sine function may be expressed as:

$$\sin^{-1} x = x + \frac{x^3}{6} + \mathcal{O}[x^5]. \quad (\text{B8})$$

Therefore, the approximation that $\sin^{-1} x \simeq x$ is valid when $(x^3/6) \ll x$ i.e. when $(x^2/6) \ll 1$. Using our maximum expression for the inverse sine argument in Equation B7, the small-angle approximation is now valid for:

Condition A

$$(a/R_*)^2 \gg \frac{2}{3} \frac{1}{(1-e)^2}. \quad (\text{B9})$$

B2.2 Accuracy of the sine small-angle approximation

Let us assume that Condition A is valid so that:

$$\sin \left(\frac{\varrho_c^2}{\sqrt{1-e^2}} \sin^{-1} \sqrt{\frac{(1 \pm p)^2 - b^2}{(a/R_*)^2 \varrho_c^2 - b^2}} \right) \\ \simeq \sin \left(\frac{\varrho_c^2}{\sqrt{1-e^2}} \sqrt{\frac{(1 \pm p)^2 - b^2}{(a/R_*)^2 \varrho_c^2 - b^2}} \right). \quad (\text{B10})$$

Next, we need to investigate when the small-angle approximation for the sine function is valid i.e. when

$$\sin \left(\frac{\varrho_c^2}{\sqrt{1-e^2}} \sqrt{\frac{(1 \pm p)^2 - b^2}{(a/R_*)^2 \varrho_c^2 - b^2}} \right) \\ \simeq \left(\frac{\varrho_c^2}{\sqrt{1-e^2}} \sqrt{\frac{(1 \pm p)^2 - b^2}{(a/R_*)^2 \varrho_c^2 - b^2}} \right). \quad (\text{B11})$$

As with the investigation of the inverse sine function, we will consider the four extreme cases of:

[1] $(1 \pm p) \rightarrow (1+p)$ and $\varrho_c \rightarrow \lim_{\omega \rightarrow \pi/2} \varrho_c$

[2] $(1 \pm p) \rightarrow (1+p)$ and $\varrho_c \rightarrow \lim_{\omega \rightarrow 3\pi/2} \varrho_c$

[3] $(1 \pm p) \rightarrow (1-p)$ and $\varrho_c \rightarrow \lim_{\omega \rightarrow \pi/2} \varrho_c$

[4] $(1 \pm p) \rightarrow (1-p)$ and $\varrho_c \rightarrow \lim_{\omega \rightarrow 3\pi/2} \varrho_c$

As before, we seek to determine the maximum of the sine function's argument with respect to (a/R_*) and e_{\max} by Monte Carlo experiments and analysis of the differentials. Generating random p, b and e values via the same method used earlier, we determine upper limits for each of the four cases, shown in Figure B2.

After conducting this analysis, we are able to derive functional upper limits on the the sine function's argument with respect to (a/R_*) and e_{\max} . From these four maxima functions, one may use the maximum of *these* to demonstrate that:

$$\frac{\varrho_c^2}{\sqrt{1-e^2}} \sqrt{\frac{(1 \pm p)^2 - b^2}{(a/R_*)^2 \varrho_c^2 - b^2}} \leq \frac{2}{(a/R_*)} \left(\frac{1+e}{1-e} \right)^{3/2} \\ \forall (0 \leq p < 1); (0 \leq b < 1-p); (0 \leq \omega < 2\pi); (0 \leq e < 1). \quad (\text{B12})$$

Armed with the above, one may now answer the question as to what range of orbits the small-angle sine approximation is valid. The Maclaurin series expansion of the inverse sine function may be expressed as:

$$\sin x = x - \frac{x^3}{6} + \mathcal{O}[x^5]. \quad (\text{B13})$$

Therefore, the approximation that $\sin x \simeq x$ is valid when $(x^3/6) \ll x$ i.e. when $(x^2/6) \ll 1$. Using our maximum expression for the sine argument in Equation B12, the small-angle approximation is now valid for:

Condition B

$$(a/R_*)^2 \gg \frac{2}{3} \frac{(1+e)^3}{(1-e)^3}. \quad (\text{B14})$$

B2.3 Summary

We have now derived the conditions under which the small-angle inverse sine approximation (Equation B9) and the small-angle sine approximation (Equation B14) are valid. It is easily shown that Condition B always leads to a harder constraint on (a/R_*) , meaning that Condition A is superfluous. Applying the small-angle approximations to Equation B5 elegantly recovers b^2 , as Kipping (2010a) stated. However, the actual limit of this approximation is now quantified as:

$$\lim_{(a/R_*)^2 \gg [2(1+e)^3]/[3(1-e)^3]} b_{\text{obs}} = b. \quad (\text{B15})$$

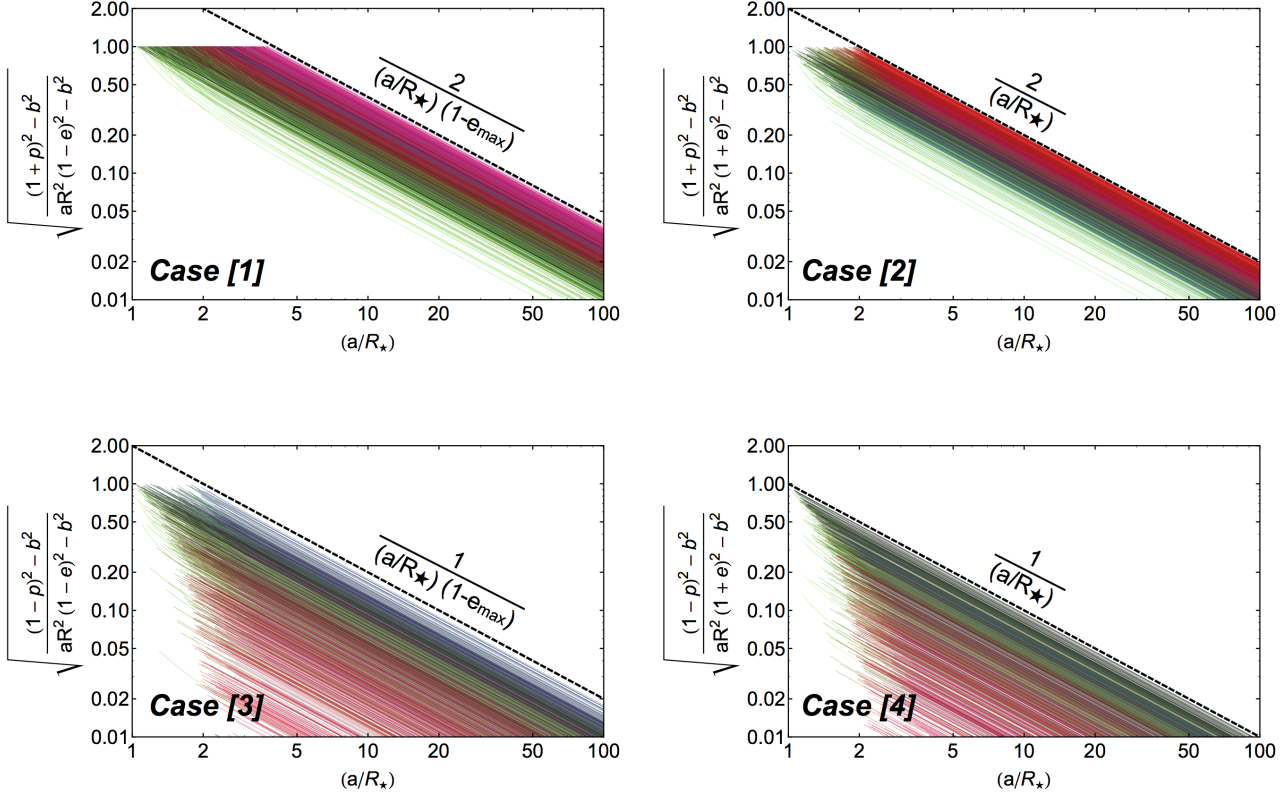


Figure B1. Small-angle inverse sine approximation investigation: On the y -axis we plot the four extreme possible arguments to the inverse sine functions present in Equation B5, with respect to (a/R_\star) on the x -axis. Each panel shows 1000 random realizations for p , b and e , where the RGB-colouring is given by $\{R, G, B\} = \{p, b, e\}$. For each panel, we show the maximum allowed value of the function in black-dashed. Simulations produced using $e_{\max} = 0.5$, but the upper limits are valid for all $0 \leq e_{\max} < 1$.

B3 Accuracy of the Density Approximation

With the valid range for assuming $b_{\text{obs}} = b$ now resolved, we may proceed to finally broach the question as to when Equation B1 is valid i.e. when the analytic model for the photo-eccentric effect can be employed. The stellar density is trivially computed from (a/R_\star) and so it is more pertinent to phrase the question as to what is $(a/R_\star)_{\text{obs}}$? Kipping (2010a) (Equation 35) showed that (without any approximation):

$$\lim_{b_{\text{obs}} \rightarrow b} (a/R_\star)_{\text{obs}}^2 = b^2 + [(1+p)^2 - b^2] \csc^2 \left[\frac{\varrho_c^2}{\sqrt{1-e^2}} \sin^{-1} \sqrt{\frac{(1+p)^2 - b^2}{(a/R_\star^2 \varrho_c^2 - b^2)}} \right]. \quad (\text{B16})$$

At this point Kipping (2010a) again invoke an inverse sine and sine small-angle approximation to simplify the above. However, making these approximations are equivalent to cases [1] & [2] of the inverse sine approximation and cases [1] & [2] of the sine function approxi-

mation made earlier in this section. Therefore, since we have already assumed Condition B (Equation B14) is in effect in order to approximate $b_{\text{obs}} = b$, then it necessarily follows that both of these small-angle approximations must also be valid. Making these approximations allows for significant simplification, yielding the same result as Equation 36 of Kipping (2010a):

$$\lim_{(a/R_\star)^2 \gg [2(1+e)^3]/[3(1-e)^3]} (a/R_\star)_{\text{obs}} = (a/R_\star) \sqrt{\varrho_c^2 \cos^2 i + \frac{(1-e^2) \sin^2 i}{\varrho_c^2}}. \quad (\text{B17})$$

The final approximation made in Kipping (2010a), which ultimately yields the photo-eccentric Ψ equation, is that the system is nearly coplanar. This essentially means that we adopt $\cos i = 0$ and $\sin i = 1$ in the above and doing so recovers Equation B1. Explicitly though, the assumption may be expressed as:

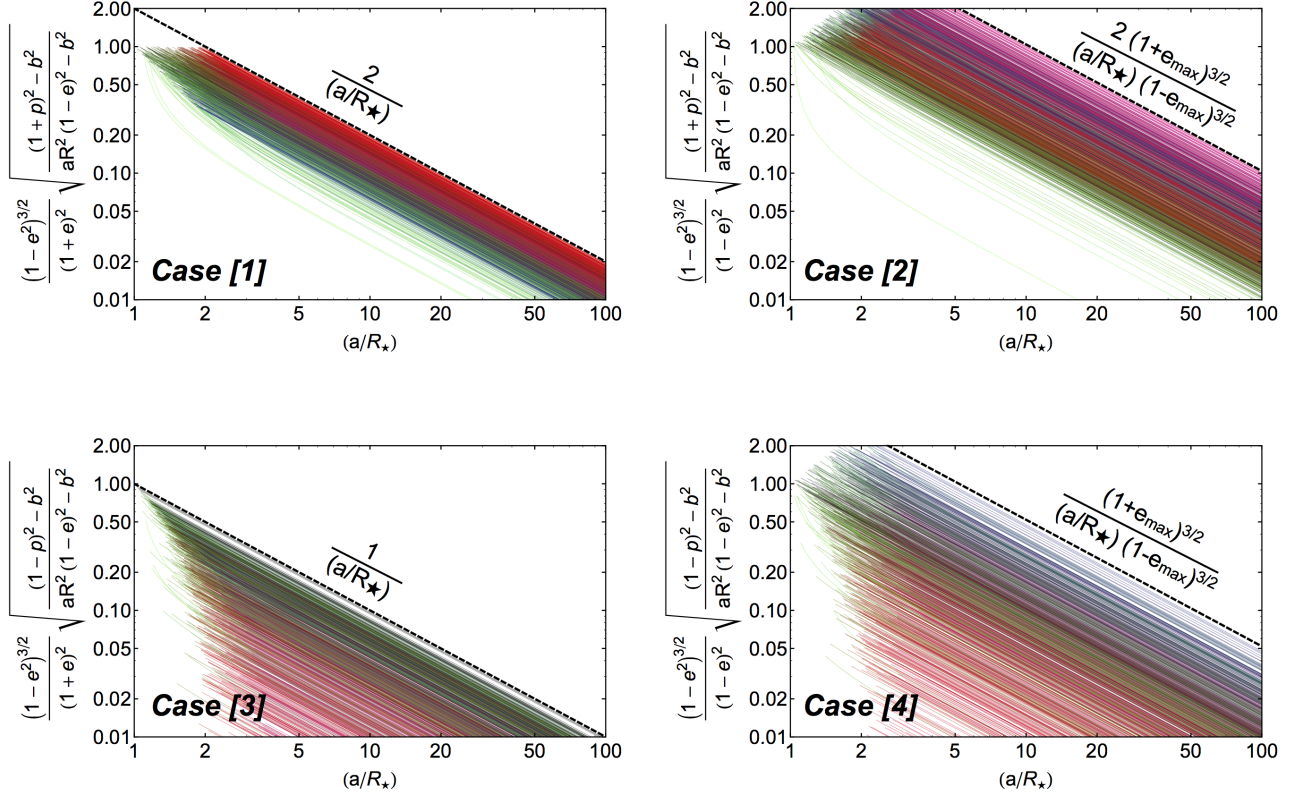


Figure B2. Small-angle sine approximation investigation: On the y-axis we plot the four extreme possible arguments to the sine functions present in Equation B5, with respect to (a/R_*) on the x-axis. Each panel shows 1000 random realizations for p , b and e , where the RGB-colouring is given by $\{R, G, B\} = \{p, b, e\}$. For each panel, we show the maximum allowed value of the function in black-dashed. Simulations produced using $e_{\max} = 0.5$, but the upper limits are valid for all $0 \leq e_{\max} < 1$.

$$\frac{1-e^2}{\varrho_c^2} \sin^2 i \gg \cos^2 i. \quad (\text{B18})$$

Replacing $\sin^2 i$ with $(1 - \cos^2 i)$ and then replacing $\cos i$ with $b/[(a/R_*)\varrho_c]$ gives:

$$(a/R_*)^2 \gg \frac{\varrho_c^4 + 1 - e^2}{1 - e^2} \frac{b^2}{\varrho_c^2}. \quad (\text{B19})$$

The function on the RHS depends upon b , e and ω and implicitly p (since $0 < b < 1 - p$). As with earlier, we seek a simple form for the maximum of the term on RHS by Monte Carlo experiment. In Figure B3, we show 1000 random realizations of this function plotted with respect to b , drawing uniform variates for $0 \leq p < 1$, $0 \leq e < e_{\max}$ and $0 \leq \omega < 2\pi$. The exercise reveals that the function is bounded by

$$\frac{\varrho_c^4 + 1 - e^2}{1 - e^2} \frac{b^2}{\varrho_c^2} \leq b^2 \left(\frac{1}{(1-e)^2} + \frac{2}{(1+e)} - 1 \right). \quad (\text{B20})$$

We may now use the above and evaluate it when $b = 1$, which maximizes the limit, to give:

Condition C

$$(a/R_*)^2 \gg \left(\frac{1}{(1-e)^2} + \frac{2}{(1+e)} - 1 \right) \quad (\text{B21})$$

Since we have assumed Condition B already, it is worth comparing the above to Equation B14. Plotting the two functions out in Figure B4 one sees that unlike the case where we compared Conditions A & B, one function does not always dominate over the other. However, the point of intersection occurs for the constraint that $(a/R_*)^2 \gg 2.2$, after which point Condition B dominates. Therefore, provided we are willing to assume the quite reasonable scenario that $(a/R_*)^2 \gg 2$ at all times, then we only need define Condition B as the defining assumption.

To summarize, the various approximations made in Kipping (2010a) may be explicitly and compactly defined by the following assumption:

$$(a/R_*)^2 \gg \frac{2}{3} \left(\frac{1+e}{1-e} \right)^3, \quad (\text{B22})$$

or equivalently this may be re-expressed in physi-

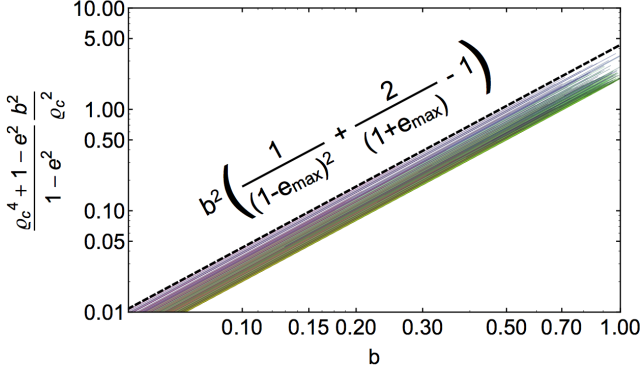


Figure B3. *Coplanar approximation investigation:* Monte Carlo realizations for the constraint on the $(a/R_\star)^2$ function, expressed on the y -axis and given in Equation B19, with respect to b . We show 1000 random realizations for the function by drawing random uniform variates for p , ω and p , which respectively define the RGB-colouring scheme. The black-dashed lined describes the observed upper limit. Simulations produced using $e_{\max} = 0.5$, but the upper limits are valid for all $0 \leq e_{\max} < 1$.

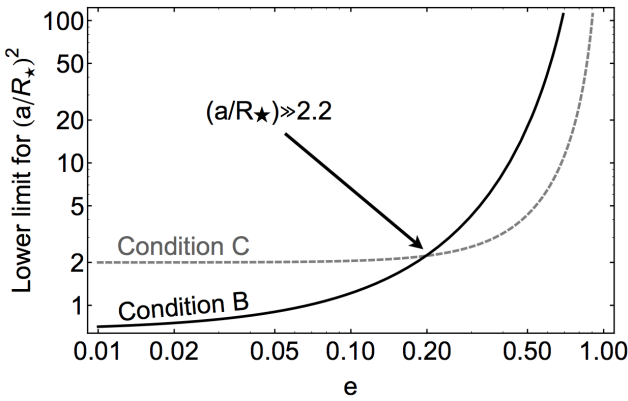


Figure B4. *Comparison of conditions B & C:* Here we plot the RHS of Equations B14&B21 in order to visualize which of the two conditions dominates. Under the reasonable assumption that $(a/R_\star) \gg 2$, then Condition B can be seen to dominate and thus we dub this the analytic photo-eccentric condition.

cal dimensions by re-writing (a/R_\star) in terms of the true stellar density

$$\left(\frac{P}{\text{days}}\right)^{4/3} \gg 0.101 \left(\frac{\rho_{\star,\text{true}}}{\text{g cm}^{-3}}\right)^{-2/3} \left(\frac{1+e}{1-e}\right)^3. \quad (\text{B23})$$

Adopting the analytic photo-eccentric condition means one may now re-write Equation B1 as

$$\lim_{(a/R_\star)^2 \gg [2(1+e)^3]/[3(1-e)^3]} \left(\frac{\rho_{\star,\text{obs}}}{\rho_{\star,\text{true}}}\right) = \Psi. \quad (\text{B24})$$

APPENDIX C: DERIVATION OF THE MINIMUM ECCENTRICITY EQUATION

In this work, we have presented a new expression for the minimum eccentricity of an exoplanet (Equation 39), as a function of the observed and true stellar densities ($\rho_{\star,\text{obs}}$ and $\rho_{\star,\text{true}}$ respectively). Here, we present a derivation of this equation. As with the other derivations in this work, we ignore other effects (e.g. photo-blend, photo-mass, etc) during the course of this derivation and assume the analytic photo-eccentric condition (Equation B23) is satisfied. Accordingly, the ratio of the observed stellar density to the true stellar density follows the expression (Kipping 2010a):

$$\left(\frac{\rho_{\star,\text{obs}}}{\rho_{\star,\text{true}}}\right) = \Psi \quad (\text{C1})$$

where

$$\Psi = \frac{(1 + e \sin \omega)^3}{(1 - e^2)^{3/2}}. \quad (\text{C2})$$

$(\rho_{\star,\text{obs}}/\rho_{\star,\text{true}})$ can therefore be seen to be a function of two parameters, e and ω , meaning that we have one observable and two unknowns. Progress can be made on this under-constrained problem by considering the extrema (i.e. the minima/maxima) of the expression. We will proceed by taking the extrema with respect to ω , which is easily achieved by computing the derivative with respect to ω . Solving $\partial(\rho_{\star,\text{obs}}/\rho_{\star,\text{true}})/\partial\omega = 0$ for ω under the condition that $0 \leq e < 1$ yields two solutions: $\omega = \pi/2$ (periapsis transit) and $\omega = 3\pi/2$ (apoapsis transit). At these extrema, we have

$$\lim_{\omega \rightarrow \pi/2} \left(\frac{\rho_{\star,\text{obs}}}{\rho_{\star,\text{true}}}\right) = \left(-1 + \frac{2}{1+e}\right)^{-3/2}, \quad (\text{C3})$$

$$\lim_{\omega \rightarrow 3\pi/2} \left(\frac{\rho_{\star,\text{obs}}}{\rho_{\star,\text{true}}}\right) = \left(-1 + \frac{2}{1+e}\right)^{3/2}. \quad (\text{C4})$$

Let us solve the above expressions so that e is the subject:

$$\lim_{\omega \rightarrow \pi/2} e = \frac{\left(\frac{\rho_{\star,\text{obs}}}{\rho_{\star,\text{true}}}\right)^{2/3} - 1}{\left(\frac{\rho_{\star,\text{obs}}}{\rho_{\star,\text{true}}}\right)^{2/3} + 1}, \quad (\text{C5})$$

and

$$\lim_{\omega \rightarrow 3\pi/2} e = \frac{(1 - \left(\frac{\rho_{\star,\text{obs}}}{\rho_{\star,\text{true}}}\right)^{2/3})(1 - \left(\frac{\rho_{\star,\text{obs}}}{\rho_{\star,\text{true}}}\right)^{2/3} + \left(\frac{\rho_{\star,\text{obs}}}{\rho_{\star,\text{true}}}\right)^{4/3})}{1 + \left(\frac{\rho_{\star,\text{obs}}}{\rho_{\star,\text{true}}}\right)^2}. \quad (\text{C6})$$

If $(\rho_{\star,\text{obs}}/\rho_{\star,\text{true}}) > 1$, then Equation C5 yields a positive eccentricity, otherwise it is negative. A negative

eccentricity of course has no meaning and this can be explained by the fact that if $\omega = \pi/2$ then it is impossible to have $(\rho_{*,\text{obs}}/\rho_{*,\text{true}}) < 1$ by simple inspection of Equation C2.

The opposite is true for Equation C6 where if $(\rho_{*,\text{obs}}/\rho_{*,\text{true}}) < 1$ then we arrive at a positive eccentricity, otherwise the derived eccentricity is negative. Again, inspection of Equation C2 reveals that one cannot have a $(\rho_{*,\text{obs}}/\rho_{*,\text{true}}) > 1$ value if $\omega = 3\pi/2$.

These two simple observations reveal the applicability of the two expressions. Specifically, if we have $(\rho_{*,\text{obs}}/\rho_{*,\text{true}}) > 1$, then we should use Equation C5 and if we have $(\rho_{*,\text{obs}}/\rho_{*,\text{true}}) < 1$ we should use Equation C6.

Finally, the two extrema can now be interpreted as the minimum eccentricity of the planet in the two distinct regimes of $(\rho_{*,\text{obs}}/\rho_{*,\text{true}}) > 1$ and $(\rho_{*,\text{obs}}/\rho_{*,\text{true}}) < 1$. This is easily verified by numerical tests and the two equations may now be combined into a single term using Heaviside Theta functions:

$$e_{\min} = \left(\lim_{\omega \rightarrow \pi/2} e \right) \mathbb{H}\left[\left(\frac{\rho_{*,\text{obs}}}{\rho_{*,\text{true}}} \right) - 1 \right] + \left(\lim_{\omega \rightarrow 3\pi/2} e \right) \mathbb{H}\left[1 - \left(\frac{\rho_{*,\text{obs}}}{\rho_{*,\text{true}}} \right) \right], \quad (\text{C7})$$

which we evaluate to be

$$e_{\min} = \left(\frac{\left(\frac{\rho_{*,\text{obs}}}{\rho_{*,\text{true}}} \right)^{2/3} - 1}{\left(\frac{\rho_{*,\text{obs}}}{\rho_{*,\text{true}}} \right)^{2/3} + 1} \right) \mathbb{H}\left[\left(\frac{\rho_{*,\text{obs}}}{\rho_{*,\text{true}}} \right) - 1 \right] + \left(\frac{\left(1 - \left(\frac{\rho_{*,\text{obs}}}{\rho_{*,\text{true}}} \right)^{2/3} \right) \left(1 - \left(\frac{\rho_{*,\text{obs}}}{\rho_{*,\text{true}}} \right)^{2/3} + \left(\frac{\rho_{*,\text{obs}}}{\rho_{*,\text{true}}} \right)^{4/3} \right)}{1 + \left(\frac{\rho_{*,\text{obs}}}{\rho_{*,\text{true}}} \right)^2} \right) \mathbb{H}\left[1 - \left(\frac{\rho_{*,\text{obs}}}{\rho_{*,\text{true}}} \right) \right], \quad (\text{C8})$$

Note that e_{\min} is purely a function of $(\rho_{*,\text{obs}}/\rho_{*,\text{true}})$ and no other terms. It is therefore possible to analytically calculate the uncertainty on e_{\min} using quadrature:

$$\sigma_{e_{\min}} = \frac{4}{3} \left(\frac{\rho_{*,\text{obs}}}{\rho_{*,\text{true}}} \right)^{-1/3} \left(1 + \left(\frac{\rho_{*,\text{obs}}}{\rho_{*,\text{true}}} \right)^{2/3} \right)^{-2} \sigma_{\rho_{*,\text{obs}}/\rho_{*,\text{true}}}, \quad (\text{C9})$$

where $\sigma_{e_{\min}}$ and $\sigma_{\rho_{*,\text{obs}}/\rho_{*,\text{true}}}$ are the uncertainties on the minimum eccentricity and $(\rho_{*,\text{obs}}/\rho_{*,\text{true}})$ observable respectively.

APPENDIX D: DERIVATION OF THE PHOTO-TIMING EFFECT

Consider $N \gg 1$ transits exhibiting periodic transit timing variations (TTV) with a period much less than the baseline of observations, such that a large number of TTV oscillations have occurred over the span of the time series. If one was unaware of these TTVs, the default assumption would be to fit a linear ephemeris model

through the transits. This is equivalent to folding the transits upon a particular linear ephemeris. Figure 3 illustrates 100 transits exhibiting sinusoidal TTVs folded in this way. The displacement of each transit from the central folded time means that when we average the light curves to produce a composite signal, this composite signal displays a different morphology to the individual transits. Specifically, the first and fourth contact points are pulled outwards and the second and third contact points are pulled inwards. This has the effect of mimicking a more grazing event and thus increases b . Since b is inversely correlated to (a/R_*) and thus ρ_* , one should anticipate that unaccounted for TTVs will produce an artificially lower ρ_* value. This may be formally proved here by considering the effect on the contact points and following the method outlined in Kipping (2010b). For a peak-to-peak TTV amplitude of $2A_{\text{TTV}}$, the contact points of the composite signal appear shifted by:

$$t_{I,\text{obs}} = t_{I,\text{true}} - A_{\text{TTV}}, \quad (\text{D1})$$

$$t_{II,\text{obs}} = t_{II,\text{true}} + A_{\text{TTV}}, \quad (\text{D2})$$

$$t_{III,\text{obs}} = t_{III,\text{true}} - A_{\text{TTV}}, \quad (\text{D3})$$

$$t_{IV,\text{obs}} = t_{IV,\text{true}} + A_{\text{TTV}}. \quad (\text{D4})$$

$$(\text{D5})$$

Together, these change the apparent transit durations, T_{23} and T_{14} , to:

$$T_{23,\text{obs}} = T_{23,\text{true}} - 2A_{\text{TTV}}, \quad (\text{D6})$$

$$T_{14,\text{obs}} = T_{14,\text{true}} + 2A_{\text{TTV}}. \quad (\text{D7})$$

Extreme scenarios can cause $T_{23,\text{obs}} < 0$ thus mimicking a grazing event, which we do not consider here. In practice, such large TTVs are easily detected and thus unlikely to go unaccounted for. Therefore, we may consider the transit depth to be unaffected and thus $p_{\text{obs}} = p_{\text{true}}$.

In order to compute the deviation in $(\rho_{*,\text{obs}}/\rho_{*,\text{true}})$ from unity due the photo-timing effect, one may follow the methodology outlined in §2.3 and feed Equation D7 into Equations 2, 3 and 4. Performing these steps yields highly elaborate expressions for $(\rho_{*,\text{obs}}/\rho_{*,\text{true}})$ and rather than formally stating the full equation (requiring many lines), meaningful insights may be drawn by plotting the resulting function for various impact parameters.

In Figure D1, we plot the ratio $(\rho_{*,\text{obs}}/\rho_{*,\text{true}})$ as a function of (A_{TTV}/P) for several iso- b contours. The plot reveals that the maximal error in $(\rho_{*,\text{obs}}/\rho_{*,\text{true}})$ occurs for $b = 0$ and so we may continue by focussing our efforts on this case and interpreting it as the maximal deviation. We find that for $(A_{\text{TTV}}/P) \simeq 10^{-5}$ the $(\rho_{*,\text{obs}}/\rho_{*,\text{true}})$ term is deviant by 1%.

$$\begin{aligned} \lim_{b \rightarrow 0} \left(\frac{\rho_{\star,\text{obs}}}{\rho_{\star,\text{true}}} \right) &= \left(\frac{3\pi}{GP^2} \right) \\ &\times \csc^3 \left[nA_{\text{TTV}} + (1+p)(a/R_{\star})_{\text{true}}^{-1} \right] \left[(1+p)^2 \right. \\ &+ \cos[nA_{\text{TTV}} + (1+p)(a/R_{\star})_{\text{true}}^{-1}] \\ &\times \left((1+p)^2 \frac{\sin^2[nA_{\text{TTV}} - (1-p)(a/R_{\star})_{\text{true}}^{-1}]}{\sin^2[nA_{\text{TTV}} + (1+p)(a/R_{\star})_{\text{true}}^{-1}]} \right. \\ &- (1-p)^2 \left. \right) \left(1 - \right. \\ &\left. \frac{\sin^2[nA_{\text{TTV}} - (1-p)(a/R_{\star})_{\text{true}}^{-1}]}{\sin^2[nA_{\text{TTV}} + (1+p)(a/R_{\star})_{\text{true}}^{-1}]} \right)^{-1} \left. \right]^{3/2}, \end{aligned} \quad (\text{D8})$$

where $n = 2\pi/P$. Making small-angle approximations of the various trigonometric terms, allows for considerable simplification of this equation:

$$\lim_{b \rightarrow 0} \left(\frac{\rho_{\star,\text{obs}}}{\rho_{\star,\text{true}}} \right) \simeq \left(\frac{p}{p + nA_{\text{TTV}}(a/R_{\star})_{\text{true}}} \right)^{3/2} \quad (\text{D9})$$

Similar small-angle approximations have been made previously in this work in Appendix B, where we derived the exact parameter range of the approximation's validity. In the case of the photo-timing effect derivation presented here, we need only concern ourselves with the $e \rightarrow 0$ limit, since our derivations consider each AP effect in isolation. The only remaining difference now is that we require $2A_{\text{TTV}} \ll T_{23}$ for the exact same approximation to be valid. Let us invoke this reasonable assumption since any large TTVs which break this condition should be easily detected and compensated for and the photo-timing effect concerns itself with clandestine timing variations. In Appendix B, we found that two conditions were required for the small-angle approximations; conditions B & C, given by Equations B14 & B21. Using those same expressions, but setting $e = 0$ as appropriate for the photo-timing derivation being considered here, we find that such an approximation is generally valid if:

$$(a/R_{\star})^2 \gg 2, \quad (\text{D10})$$

$$2A_{\text{TTV}} \ll T_{23}. \quad (\text{D11})$$

which can be considered to be true for the vast majority of orbital configurations. As visible from Figure D1, the approximation given by Equation D9 does an excellent job of reproducing the behavior of the exact solution for $b = 0$. This equation is also highly practical in estimating the error in $(\rho_{\star,\text{obs}}/\rho_{\star,\text{true}})$ when some upper limit on the TTVs has been derived, since the $b = 0$ limit is the most conservative case and in general the derived b will over-estimated and thus unreliable anyway due to the TTV smearing. This TTV smearing imposes a fundamental limit on the precision at which one can measure $(\rho_{\star,\text{obs}}/\rho_{\star,\text{true}})$.

To make Equation D9 of even greater practical value to observers, it is useful to replace $(a/R_{\star})_{\text{true}}$ with $\rho_{\star,\text{true}}$ since this parameter is more directly inferred from an independent measure of the star. Further, in the case of no detected TTVs, the A_{TTV} may be replaced with the upper limit on the TTV amplitude and the LHS may be interpreted as the uncertainty in $(\rho_{\star,\text{obs}}/\rho_{\star,\text{true}})$:

$$\sigma_{(\rho_{\star,\text{obs}}/\rho_{\star,\text{true}})}^{\text{max}} = 1 - \left(1 + \frac{2\pi^{2/3}}{3^{1/3}} \frac{G^{1/3} \rho_{\star,\text{true}}^{1/3}}{pP^{1/3}} \sigma_{A_{\text{TTV}}} \right)^{-3/2}, \quad (\text{D12})$$

where

$$\sigma_{(\rho_{\star,\text{obs}}/\rho_{\star,\text{true}})} \leq \sigma_{(\rho_{\star,\text{obs}}/\rho_{\star,\text{true}})}^{\text{max}} \quad (\text{D13})$$

and $\sigma_{A_{\text{TTV}}}$ is the 1σ upper limit on the presence of TTVs. For $N \gg 1$ transits observed with an approximately constant timing precision of σ_{τ} , one expects the standard deviation of the TTV points in the absence of a signal to be σ_{τ} . The uncertainty on this prediction (i.e. the standard deviation of the standard deviation) is given by $\sigma_{\tau}/\sqrt{2(N-1)}$ assuming normally distributed errors. The 1σ maximum standard deviation can then be compared to that expected from an embedded sinusoid within the data which could cause a standard deviation of $\sqrt{\sigma_{\tau}^2 + (A^2/2)}$:

$$\sqrt{\sigma_{\tau}^2 + (A^2/2)} = \sigma_{\tau} + \sigma_{\tau}/\sqrt{2(N-1)}. \quad (\text{D14})$$

Solving for A gives $\sigma_{A_{\text{TTV}}}$ as

$$\sigma_{A_{\text{TTV}}} = \sigma_{\tau} \sqrt{\frac{1}{N-1} + \sqrt{\frac{8}{N-1}}}, \quad (\text{D15})$$

$$\lim_{N \gg 1} \sigma_{A_{\text{TTV}}} \simeq \sigma_{\tau} \left(\frac{8}{N} \right)^{1/4}. \quad (\text{D16})$$

We may now plug the above result into Equation D12. Further, we take an approximate estimate of the $\rho_{\star,\text{true}}$ term on the RHS of Equation D12 to be equal to $\rho_{\star,\text{obs}}$. Finally, we assume that the fractional error is much less than unity to simplify the expression to

$$\sigma_{(\rho_{\star,\text{obs}}/\rho_{\star,\text{true}})}^{\text{max}} \simeq 7.5 \frac{G^{1/3} \rho_{\star,\text{obs}}^{1/3}}{pP^{1/3}} \frac{\sigma_{\tau}}{N^{1/4}}. \quad (\text{D17})$$

In a Taylor expansion of $[1 - (1+x)^{3/2}]$, we require $x \ll 0.8$ for Equation D17 to be applicable, which corresponds to:

$$\left(\frac{P}{\text{days}} \right)^{1/3} \gg \frac{1}{150p} \left(\frac{A_{\text{TTV}}}{\text{seconds}} \right) \left(\frac{\rho_{\star,\text{true}}}{\text{g cm}^{-3}} \right)^{-1/3}. \quad (\text{D18})$$

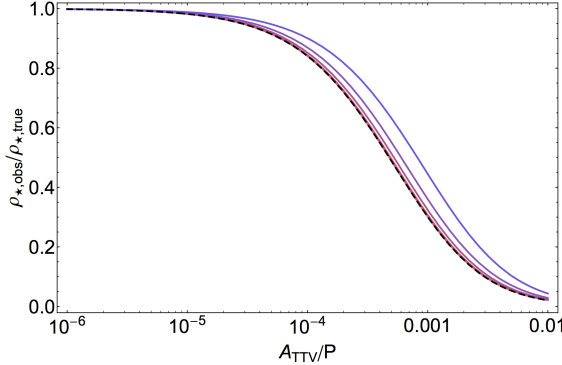


Figure D1. The effect of unaccounted for transit timing variations (x-axis) on the observed mean stellar density (y-axis) from a composite transit light curve. From red to blue we show iso-\$b\$ contours of \$b = 0.0, 0.2, 0.4, 0.6 \& 0.8\$ respectively. The black-dashed line shows the result of our approximate expression in the \$b = 0\$ limit (Equation D9). Realizations computed using \$P = 10\$ days, \$\rho_{\star} = \rho_{\odot}\$ and \$p = 0.1\$.

APPENDIX E: DERIVATION OF THE PHOTO-DURATION EFFECT

Consider a planet undergoing periodic, low-amplitude velocity-induced transit duration variations (TDVs). By periodically increasing/decreasing the velocity of a planet, one expects the transit duration to scale inversely. In Figure 4, the effect is illustrated on the composite light curve.

The outcome of unaccounted TDVs is similar to that of unaccounted TTVs. Namely, the first and fourth contacts are pulled outwards and the second and third contacts are pulled inwards. Thus one should expect unaccounted TDVs to cause one to underestimate the stellar density, like TTVs.

In what follows we consider the effect of a sinusoidal velocity variation via

$$v(t) = v_0[1 - A_{\text{TDV}} \sin(2\pi t/P_{\text{TDV}})]. \quad (\text{E1})$$

However, it is important to note the derivation is general for any periodic waveform and in this sense our models defines \$A_{\text{TDV}}\$ as half of the peak-to-peak velocity variation amplitude. Since \$T_{23}^{14}\$ is linearly inversely proportional to the velocity, \$v\$, then we have:

$$T_{23}^{14}(t) = T_{23}^{14,0}[1 - A_{\text{TDV}} \sin(2\pi t/P_{\text{TDV}})]^{-1}. \quad (\text{E2})$$

If \$A_{\text{TDV}} \ll 1\$, then we have:

$$T_{23}^{14}(t) \simeq T_{23}^{14,0}[1 + A_{\text{TDV}} \sin(2\pi t/P_{\text{TDV}})] \quad (\text{E3})$$

In such a case, one can show that the composite contact points are shifted by

$$t_{I,\text{obs}} = t_{I,\text{true}} - A_{\text{TDV}} T_{14,0}, \quad (\text{E4})$$

$$t_{II,\text{obs}} = t_{II,\text{true}} + A_{\text{TDV}} T_{23,0}, \quad (\text{E5})$$

$$t_{III,\text{obs}} = t_{III,\text{true}} - A_{\text{TDV}} T_{23,0}, \quad (\text{E6})$$

$$t_{IV,\text{obs}} = t_{IV,\text{true}} + A_{\text{TDV}} T_{14,0}. \quad (\text{E7})$$

$$(\text{E8})$$

Together, these change the observed transit durations, \$T_{23}\$ and \$T_{14}\$, to:

$$T_{23,\text{obs}} = T_{23,\text{true}} - 2A_{\text{TDV}} T_{23,\text{true}}, \quad (\text{E9})$$

$$T_{14,\text{obs}} = T_{14,\text{true}} + 2A_{\text{TDV}} T_{14,\text{true}}. \quad (\text{E10})$$

One may now proceed to derive the effect on \$\rho_{\star,\text{obs}}\$ as we did before for the photo-timing effect. However, unlike the photo-timing effect, we find that a simple form of the equation is possible for all \$b\$ values, given by:

$$\left(\frac{\rho_{\star,\text{obs}}}{\rho_{\star,\text{true}}} \right) = \left(\frac{(a/R_{\star})^2 p + 4A_{\text{TDV}}^2 b^2 p + 2A_{\text{TDV}}[(1-p^2)^2 - b^2(1+p^2)]}{(a/R_{\star})^2 [p + 4A_{\text{TDV}}^2 p + 2A_{\text{TDV}}(1+p^2-b^2)]} \right)^{3/2}, \quad (\text{E11})$$

where \$(a/R_{\star})\$ is \$(a/R_{\star})_{\text{true}}\$ and can be estimated as \$[(GP^2\rho_{\star})/(3\pi)]^{1/3}\$. As with the previous derivations, the above required making similar small-angle approximations to those made in Appendix B. These approximations are valid here too under the already made assumption that \$A_{\text{TDV}} \ll 1\$, meaning we assume:

$$(a/R_{\star})^2 \gg 2, \quad (\text{E12})$$

$$A_{\text{TDV}} \ll 1. \quad (\text{E13})$$

This paper has been typeset from a TeX/ L^AT_EX file prepared by the author.